Pharmacological PIK3C2B inhibition rescues XLMTM phenotype in mouse models and identifies molecular markers of disease

Andrew Shearer[1], Melissa L. Brooks[1], Maxine M. Chen[1], Thiwanka Samarakoon[1], John Hsieh[1], Gramoz Kondakci[1], Emanuele Perola[1], Jason Brubaker[1], Kristina Fetalvero[1], Stefanie Schalm[1,2], Joana Caetano-Lopes[1,*]

[1]Blueprint Medicines Corporation, Cambridge, MA, USA. [2]Bayer Research & Innovation Center, Cambridge, MA, USA.

*Corresponding author

45 Sidney St, Cambridge, MA 02139
+ 1 503-679-8617
Email address: rclopes.j@gmail.com

Total word count: 11,210

Total number of figures and tables: 8 main (7 figures/1 table), 7 supplemental

Keywords: Neuromuscular diseases, protein kinases, drug therapy

Conflict of interest statement: All authors were employees of Blueprint Medicines, a Sanofi company, at the time of the reported work.

Abstract

X-linked myotubular myopathy (XLMTM) is a rare genetic disorder that typically presents at birth with progressive muscle weakness and respiratory difficulties and is caused by myotubularin 1 (*MTM1*) gene mutations. Here, we examine the role of phosphatidylinositol-4-phosphate 3-kinase catalytic subunit type 2 beta (PIK3C2B), a lipid kinase that interacts with MTM1, in XLMTM in various models. We examined the effect of BLU3797, a novel, highly potent, selective, orally bioavailable PIK3C2B inhibitor, on survival, muscle development, myofiber phenotypes, and gene expression in *MTM1*$^{-/y}$ mice. PIK3C2B-deficient XLMTM animals demonstrated increased survival, restored muscle function, fewer myofibers with centralized nuclei, and normalization of disease-associated molecular markers. BLU3797 alleviated the XLMTM phenotype in a dose-dependent and reversible manner. Loss of functional PIK3C2B in XLMTM mice promoted a more differentiated, adult-like myofiber profile, which was strongly associated with normalization of disease surrogates and a reduction in markers of early muscle development and regeneration. BLU3797 treatment appears to modulate the expression of microRNAs associated with satellite cell activation and myofiber fusion. These findings indicate that PIK3C2B inhibition with BLU3797 effectively reverses the XLMTM disease phenotype by enhancing muscle function and promoting development toward a more mature state.

Word count: 192/200

Introduction

X-linked myotubular myopathy (XLMTM) is a rare genetic disorder with an estimated prevalence of one in 50,000 male births and is characterized by profound muscle weakness and respiratory challenges (1). XLMTM primarily affects males, with symptoms typically appearing at birth or in early infancy. Affected

individuals exhibit profound muscle weakness, leading to difficulties with movement and motor skills. Hypotonia, or low muscle tone, is a common feature, resulting in floppiness and poor muscle control (2-6). Respiratory complications, such as breathing difficulties and frequent respiratory infections, are also prevalent in XLMTM patients (4-8). Additionally, patients may experience hepatobiliary disease, feeding difficulties, delayed or loss of motor milestones, and skeletal abnormalities, among other issues (4-6, 8-10). Supportive therapies, including respiratory support, physical therapy, and nutritional interventions, play a crucial role in symptom management and promoting overall well-being. These interventions offer much-needed progress in addressing the challenges associated with XLMTM and improving the lives of those affected by the condition (4, 5, 8, 11). Despite advances in disease intervention and supportive care, there is currently no cure for XLMTM, warranting the need to develop curative therapies.

The underlying cause of XLMTM is deleterious mutations in the myotubularin 1 (*MTM1*) gene that result in loss of function or altered expression of myotubularin, a lipid phosphatase. To date, over 300 mutations in the *MTM1* gene have been identified (2, 12-18). Although information on genotype-phenotype relationships is limited, truncating mutations typically result in a more severe phenotype, while non-truncating mutations outside the catalytic domain of myotubularin have been associated with milder presentations (2, 12, 14, 15, 19-21). Myotubularin is a broadly expressed phosphatase that plays a critical but cryptic role in muscle development and function (16). The essential function of myotubularin and its orthologs in regulating phosphatidylinositol 3-phosphate (PtdIns3P), endocytosis, and endo(lyso)somal function has been extensively studied in various model organisms, including *Drosophila*, *C. elegans*, zebrafish, mice, and higher mammals (16). These models have provided valuable insights into the role of myotubularin and have contributed to our understanding of myotubularin deficiency (22). The major enzymatic function of myotubularin is to dephosphorylate PtdIns3P and phosphatidylinositol 3,5-bisphosphate, which are important phosphoinositides involved in membrane trafficking and signaling

(20, 23-25). Mutations in the *MTM1* gene lead to a deficiency or dysfunction of myotubularin, disrupting normal muscle cell maturation and function (26). Deficiency of myotubularin has also been linked to elevated mTORC1 activity, leading to a disruption in the connection between starvation and the initiation of autophagy (27).

Several physiological changes are observed in the muscle tissues of MTM1-deficient animal models and human patients. The *MTM1* knock-out (KO) mouse differs from the human disease phenotype by exhibiting muscle weakness and atrophy primarily during the post-natal period, implying that myotubularin deficiency may primarily affect muscle growth and maintenance rather than muscle development in these mice (22). The *MTM1*p.R69C mouse model was generated by introduction of a point mutation (c.205C>T) to exon 4 of *MTM1*, resulting in a loss of *MTM1* full-length messenger RNA (mRNA) expression, and animals exhibited early muscle atrophy and muscle weakness at 2 months of age. Similar to the KO model, histopathological analysis revealed small myofibers with centrally located nuclei, which is a characteristic feature observed in the human disease (28). The exact mechanisms by which *MTM1* mutations cause XLMTM are still being elucidated, but it is believed that impaired membrane trafficking, abnormal muscle fiber formation, and altered signaling pathways contribute to the disease phenotype (23, 26, 29, 30).

A reciprocal interplay has been demonstrated between MTM1 and the phosphoinositide 3-kinase (PI3K) enzyme family (20, 31). Phosphatidylinositol-4-phosphate 3-kinase catalytic subunit type 2 beta (PIK3C2B) is a ubiquitously expressed member of the PI3K family that plays a critical role in intracellular signaling pathways. PIK3C2B catalyzes the phosphorylation of phosphatidylinositol (PtdIns) and PtdIns4P, generating PtdIns3P and PtdIns(3,4)P2, which serve as important signaling molecules within the cell (32). The relationship between PIK3C2B and MTM1 was initially established through *in vivo* experiments, where mice deficient for both MTM1 and PIK3C2B had no observable disease phenotype (31, 33). A

recent study indicates that MTM1 and PIK3C2B both metabolize a shared pool of PtdIns3P within endosomal compartments. In the absence of MTM1, PtdIns3P accumulates on vesicles positive for early endosome antigen 1 (EEA1), while depletion of PIK3C2B helps restore PtdIns3P levels (34). These observations highlight the pivotal role of MTM1 in regulating a distinct pool of PtdIns3P.

Here, we present additional *in vitro* and *in vivo* data that further support the role of PIK3C2B inhibition in reversing XLMTM symptoms in a mouse model and describe the downstream impacts of PIK3C2B inhibition on gene expression alterations that may impact development of the disease phenotype.

Results

BLU3797 is a selective and potent PIK3C2B inhibitor

An internal discovery program targeting inhibition of PIK3C2B led to the synthesis of inhibitors with various degrees of potency and selectivity. Two of these inhibitors, BLU3797 and BLU2720, were extensively characterized in a series of in vitro and in vivo studies.

BLU3797 showed high selectivity for PIK3C2B while sparing other PI3K family members and pharmacokinetic properties that would furnish *in vivo* exposures in mice achieving C_{trough} = PIK3C2B IC_{50} over a 24-hour period utilizing a single orally administered dose. BLU2720 posesses physicochemical properties and selectivity similar to BLU3797 as assessed biochemically (Figure 1B). Further evaluation of BLU3797 (Figure 1C) and BLU2720 (Figure 1D) by NanoBRET™ revealed levels of selectivity similar to those observed biochemically (Table 1). BLU3797 has low affinity for other kinases in general as assessed by kinome scan (Figure 1E), with an overall S(10) selectivity score of 0.015. Taken together these data imply that BLU3797 is a potent and highly kinome sparing inhibitor of PIK3C2B.

BLU3797 treatment increases MTM1-null myotube nuclear density

C2C12 cells are a common cell model to evaluate muscle development and when engineered to lack MTM1 expression have, in previous publications (35), been shown to have reduced myogenic potential. Our own generation of a series of *MTM1*-null clones showed heterogeneity in terms of myogenic identity even as myoblasts (Supplemental Figure 1). Control clones that had been transfected with non-targeting single-guide RNA (sgRNA) showed signs of lost myogenic identity (low Pax7 and myogenin protein levels) and showed limited fusion (data not shown) when differentiated.

A single clone exhibiting both acceptable lineage commitment and fusion competence was selected for further analysis. Mass spectrometry of undifferentiated C2C12 cells confirmed that MTM1 was present in wild-type (WT) cells but absent in the *MTM1*-null cells (Figure 2A). In *MTM1*-null cells, there was a marked increase in PAX7 expression and more moderate increases in myogenin (MYOG) and MYOD, findings that were corroborated by western blot analysis (Figure 2B). Upon differentiation, MYOG levels increased in both WT and *MTM1*-null cells, treatment with BLU3797 or BLU2720 did not affect these levels. WT and *MTM1*-null cells transduced with shRNA targeting *Pik3c2b* resulted in a 50% reduction in PIK3C2B expression. After five days of differentiation, *MTM1*-null myotubes appeared wider compared to WT cells. Additionally, and in line with previously published data (36), *MTM1*-null cells showed reduced terminal differentiation, as indicated by an apparent lower number of multinucleated myotubes, a phenotype that was improved by *Pik3c2b* shRNA (Figure 2C). We then used *MTM1*-null cells to create an assay that would evaluate if there was any effect upon fusion, or terminal differentiation, with a PIK3C2B inhibitor (Figure 3A). Treatment with BLU3797 increased the fusion index, the number of nuclei within sarcomeric myosin positive objects, in a dose-dependent fashion (Figure 3B). While there appeared to be an increase in this metric with BLU2720 as well, the change from baseline was not as significant, reflecting the difference in potency of PIK3C2B-inhibition between the 2 molecules (Figure

3C). There was also a significant, dose-dependent increase in the average number of nuclei per myotube. Overall, the greatest increase in myotube nuclei was observed at the 188 nM concentration, suggesting that higher doses did not provide additional benefit. In contrast to BLU3797, treatment with BLU2720 did not result in a substantial increase in nuclei per myotube. Intriguingly, the total number of myotubes in the BLU3797 treated conditions decreased in a dose-dependent manner. This reduction was inversely related to the increase in myonuclear number, a pattern not observed with BLU2720. As expected, these trends were absent in *MTM1*-null cells with *Pik3c2b*-knockdown (Supplemental Figure 2), suggesting that the observed effects are specifically associated with PIK3C2B inhibition.

PIK3C2B loss of function rescues the disease phenotype in the MTM1$^{-/-}$ mouse model

We generated a kinase-dead (D1212A) PIK3C2B-expressing mouse to assess the effect of global PIK3C2B activity reduction (Supplemental Figure 3A). As expected, introduction of the *D1212A* mutation (Supplemental Figure 3B) did not affect PIK3C2B protein expression (Supplemental Figures 3C-D) and had no impact on mouse survival, gross phenotype, weight (Supplemental Figure 3E), or fertility. This mouse strain was then bred with the *MTM1*$^{-/y}$ mouse line to better understand the extent of rescue that would be expected from treatment with a PIK3C2B-selective inhibitor. As reported by other groups (31, 33), there was a profound rescue of the disease phenotype with loss of kinase activity. Specifically, loss of functional PIK3C2B in the context of XLMTM led to the restoration of normal growth (Figure 4A) and muscle function as assessed by wire hanging (Figure 4B). Additionally, we observed that the gait of XLMTM animals lacking functional PIK3C2B was restored to resemble that of WT controls (Figure 4C).

In addition to the improvements in growth and muscle function there was also a near-complete improvement in the histological phenotypes observed in XLMTM (Figure 4D). The percentage of myofibers with centralized nuclei, a common marker of XLMTM, was elevated in mice deficient for MTM1 and this elevation was fully reduced to WT levels in animals that were also deficient for PIK3C2B

activity (Figure 4E). A similar effect was also observed for myofibers, where the diameter was decreased in MTM1-deficient mice compared with WT controls but was increased back to that of WT controls by the lack of PIK3C2B activity (Figure 4F). Because the myofiber diameter is reduced in *MTM1*$^{-/y}$ mice, there is also an observed increase in the number of nuclei per unit of area, which was fully corrected by the loss of functional PIK3C2B (Figure 4G). The overall cross-sectional area of myofibers was also revealed to be significantly decreased in *MTM1*$^{-/y}$ mice relative to WT, and this phenotype was largely corrected by loss of functional PIK3C2B (Figure 4H). Both the histological and functional data indicated that loss of functional PIK3C2B corrected the XLMTM-associated muscle phenotype. We then investigated changes in molecular markers of disease to further understand this effect.

Previous work has demonstrated that myostatin, an inhibitor of muscle growth, levels are decreased in both the plasma and muscle tissue of animal models of centronuclear myopathies, including XLMTM (37). Indeed, *MTM1*$^{-/y}$ mice showed a decrease in plasma myostatin levels that was restored to WT levels with loss of PIK3C2B activity (Figure 4I). The marker PtdIns3P, which is known to be elevated in *MTM1*-null muscle, was fully reduced by loss of PIK3C2B activity (Figure 4J). An additional marker commonly seen in *MTM1*$^{-/y}$ is the accumulation of SQSTM1/P62 owing to stalled autophagy. SQSTM1/p62 is a key selective autophagy receptor that recognizes and binds ubiquitinated protein aggregates and damaged organelles. Its levels also serve as an indicator of autophagic flux, with accumulation reflecting impaired autophagy (38). Indeed, SQSTM1/P62 protein levels were significantly increased in *MTM1*-null animals but reduced to WT levels with the loss of functional PIK3C2B (Figure 4K).

Loss of PIK3C2B in MTM1*$^{-/y}$ *animals led to notable alterations in metabolic myogenic proteins

Proteomic and phosphoproteomic analyses using mass spectrometry were performed to uncover additional changes and identify potential disease-relevant markers (Supplemental Figure 4). Both *in vitro* and *in vivo* findings suggested that there was an increase in myogenesis or, at least, an accumulation of larger myofiber or myotubular structures, following the loss of PIK3C2B activity. Unexpectedly, loss of

PIK3C2B activity in *MTM1*$^{-/y}$ animals led to a noticeable decrease in myogenic markers (Figure 5A, B), accompanied by an increase in proteins associated with particular types of metabolism. This pattern has also been reported by others (39, 40) and is generally used to distinguish developing or regenerating muscle tissue. In line with these findings, we observed decreased phosphorylation (Figure 5C, D) of contractile proteins and calcium-mobilizing factors. Similar changes have also been documented in XLMTM diseases models (41) and are thought to reflect maladaptive remodeling of contractile structures. Collectively, these results suggest that loss of PIK3C2B activity in XLMTM muscle promotes normal tissue maturation without impacting lineage commitment.

Increased PtdIns3P levels have been used to generally describe the underlying mechanism behind the development of the XLMTM disease phenotype. Additional studies, largely *in vitro*, have found the nature of PIK3C2B-related PtdIns3P levels to be highly contextual and spatially restricted within the cell (31, 34). Phosphatidylinositol 3-kinase catalytic subunit type 3 (PIK3C3), or VPS34, is a lipid kinase that is involved not only in the synthesis of PtdIns3P but also in endomembrane dynamics, but unlike PIK3C2B, the loss of PIK3C3 results in loss of embryonic viability (31). We performed lipidomic profiling of WT and *PIK3C3*$^{-/-}$ C2C12 cells with and without PIK3C2B compound treatment, and identified 21 lipids in these cell lines, including phospholipids (n = 14), sphingolipids (n = 3), glycerolipids (n = 2), and sterolipids (n = 2). Treatment of WT C2C12 cells with BLU3797 had minimal impact on overall lipid composition, whereas loss of PIK3C3 resulted in a pronounced alteration of the cellular lipid profile (Figure 5E). The addition of BLU3797 further modified the lipid profile, resulting in an intermediate phenotype that clustered between WT and *PIK3C3* KO cells without treatment. Comparison of the differential abundance profiles between BLU3797 treatment and no treatment in *PIK3C3* KO cells vs. *PIK3C3* WT cells show that, unlike the lack of significant treatment effect in the *PIK3C3* WT cells, a PIK3C2B inhibitor significantly changes (7/21, 33%) the lipid groups profiled compared with no treatment in the *PIK3C3* KO cells (Figure 5F).

Selective inhibition of PIK3C2B effectively rescues the MTM1-null phenotype

MTM1$^{-/y}$ mice were backcrossed with C57BL/6 WT mice over several generations, resulting in a genetic background that was 70% C57BL/6 as determined by single nucleotide polymorphism (SNP) analysis. This shift led to a marked increase in disease severity and a decrease in animal survival compared to previously published studies (42). Animals began to succumb to disease around the time of weaning (postnatal day 21), with most requiring humane euthanasia within 2-3 days afterward. This period of mouse development is characterized by marked muscle growth, including myofiber lengthening, physiological hypertrophy, and fiber type maturation occurring near simultaneously (43-45). This shift in background created a more pronounced form of the disease, similar to what has been observed in other muscle-related diseases (42, 46). We generated a conditional version of this model, which did not result in loss of viability or the XLMTM disease phenotype. However, it did show a reduction in myofiber diameter and an increase in the fraction of myofibers with centralized nuclei (Supplemental Figure 5).

Due to the constraints associated with this model's survival, we adapted our *in vivo* studies to begin at post-natal day 22. Increasing daily doses of BLU3797 (25, 50, 100 mg/kg) all seemed to surpass the NanoBRET™ calculated IC_{50} (Figure 6A) and led to a marked improvement in animal survival through the end of the study (Figure 6B). Animals treated with compound gained weight and developed in a fashion similar to WT controls whereas untreated *MTM1*$^{-/y}$ animals showed a failure to thrive, as evidenced by their inability to gain weight, requiring humane euthanasia (Figure 6C). All treated groups showed improvement in wire hanging latency with the degree and durability of this effect showing a strong dose dependency (Figure 6D). Analysis of tissue sections also found a dose-dependent decrease in the number of myofibers with centralized nuclei to the level of WT tissue (Figure 6E). Further analysis revealed a modest increase, but not a full rescue, in myofiber diameter (Figure 6F). Compound treatment normalized the level of plasma myostatin (Figure 6G) and the level of muscle SQSTM1/P62 ,

as detected by ELISA (Figure 6H). We further investigated whether daily dosing was needed to rescue the XLMTM phenotype by dosing animals once every 48 hours at 50 or 100 mg/kg. As expected, both groups showed a significant improvement in survival (Figure 6I), which was persistent in the higher dose group but began to wane in the 50 mg/kg group. By the end of the study, *MTM1*$^{-/y}$ animals treated with 100 mg/kg of BLU3797 had a 100% survival rate, while those treated with 50 mg/kg had a 20% survival rate.

We next considered whether the durability and extent of rescue were not only dose-dependent, but also influenced by the timing of treatment initiation. In a small-scale study, animals started on treatment either just after weaning (22 days of age) or at the typical time of euthanasia (25 days of age), receiving twice-daily doses of 75 mg/kg BLU3797 to achieve C_{trough} at the NanoBRET™-derived 90% inhibitory concentration (IC_{90}). This regimen resulted in rescued viability and improved muscle function (Supplemental Figure 6A-D). After treatment, animals were withdrawn from the compound and monitored until humane euthanasia was required. The decline in muscle function following the final dose was highly similar between the 2 groups. Myostatin levels in the D25 group were lower than those in the D22 group yet remained improved compared to the vehicle-treated group (Supplemental Figure 5E). Curiously, even after compound withdrawal, SQSTM1/P62 levels remained significantly reduced at the end of the study (Supplemental Figure 5F). This finding indicates that similar results are achieved whether the animals are dosed preventively or therapeutically.

Micro-RNA analysis of tissues

Our data suggests that there is a critical window during muscle development when PIK3C2B inhibition is effectiveand fully reversible. Identifying dynamic markers of disease has been challenging, and those currently used are somewhat tangential to the disease phenotype (e.g., SQSTM1/P62). MicroRNAs (miRNAs) have been put forward as potential markers to assess disease severity. Therefore, we examined how the muscle miRNA profile changes under different treatment conditions in the context of

the disease phenotype. To accomplish this, we treated WT and XLMTM animals with BLU3797 every 36 hours (Q36h), starting at day 22 of age, administering either 5 or 3 doses (Figure 7A). Comparisons between WT and XLMTM were complicated by the large number of miRNAs that showed differential expression. Comparing the miRNA profiles of animals that received continuous treatment (5 doses) with those that underwent withdrawal (3 doses) revealed a smaller set (15) of differentially expressed miRNAs (Figure 7B). Of the 15 identified miRNAs, 9 (miRNAs: 103, 107, 324-5p, 145, 30a, 1198, 125a-3p, 26a, 490) were increased in the 5-dose group compared to the 3-dose group. The remaining 6 miRNAs were decreased in the 5-dose group relative to the 3-dose group (miRNAs: 802, M55-1, 292-5p, 511 2133, 1186b). We were particularly interested in six miRNAs whose expression levels in the 5-dose group matched those of the WT group, but were differentially modulated in the 3-dose group (miRNAs: 103, 107, 324-5p, 145, 30a, 26a). We then focused on those miRNAs for which commercially available quantitative polymerase chain reaction (qPCR) kits were available (Figure 7C). Of the selected miRNAs, 3 have human homologs known to be involved in muscle development and maturation (30a-3p, 30a-5p, and 26a-5p) (47-49), while the other 3 appeared to have a less clearly defined role in muscle development (324-5p, 107, and 145-3p) (50-52). All 6 miRNAs were found to be increased in the 5-dose group relative to the 3-dose group, confirming our initial screening results.

To gain deeper mechanistic insight into how the loss of miRNA expression may contribute to the disease phenotype, we focused on the expression of secreted frizzled-related protein 1 (SFRP1) and suppressor of mothers against decapentaplegic protein 1 *(*SMAD1*).* SFRP1 has been shown to inhibit myotube formation in both C2C12 cell cultures and primary muscle tissue and is believed to be regulated by miR-30a-3p (53-55). SMAD proteins are known to play a role in muscle development, and the overexpression of SMAD1 has been shown to inhibit muscle cell differentiation (56). Consistent with the reduction in suppressive miRNAs, transcript levels of both genes were significantly elevated in the XLMTM

withdrawal group but decreased with continuous BLU3797 treatment (Figure 7D, E).. SFRP1 protein levels in muscle, assessed by ELISA, were reduced in the continuous dosing group relative to the withdrawal group (Figure 7F). Building on these findings, we observed that *Sfrp1* transcript levels were increased in our *MTM1*-null C2C12 cells, and this increase is partially corrected with BLU3797 treatment (Figure 7G). While *Smad1* mRNA, but not SMAD1 protein, levels were significantly modulated by continuous treatment(Figure 7H, I). Collectively, these data suggest that the identified miRNAs are part of a broader regulatory mechanism. When dysregulated in XLMTM, this leads to increased expression of factors that can impact terminal differentiation of myoblasts, a process that can be corrected through PIK3C2B inhibition.

Discussion

In this study, we developed a potent and selective PIK3C2B inhibitor that phenocopied the loss of functional PIK3C2B by dramatically rescuing the XLMTM phenotype in mice... In both models, XLMTM animals with deficient PIK3C2B activity exhibited increased survival, restored muscle function, fewer myofibers with centralized nuclei, and normalized disease-associated molecular markers (SQSTM1/P62 and myostatin). The improvements observed with BLU3797 treatment were dose-dependent and reversible, supporting the conclusion that inhibition of PIK3C2B kinase activity can effectively rescue the XLMTM phenotype.

We found that *MTM1*-null C2C12 cells, regardless of PIK3C2B depletion, exhibited similar levels of lineage commitment. However, *MTM1*-null cells with PIK3C2B depletion showed an increased number of nuclei per myotube. Consistent with this, treatment with BLU3797 significantly increased the number of nuclei per myotube, accompanied by a modest but significant decrease in the number of unique myotubes. This suggests that enhanced myotube-myotube and terminal myoblast-myotube fusion

289 contribute to this effect. It is therefore not surprising that the critical period when PIK3C2B activity is
290 most detrimental, and when its inhibition is most disease modifying,

291 The precise role of PIK3C2B in XLMTM disease progression is linked to excessive PtdIns3P production,
292 though this effect may be limited to specific spatial or contextual settings. Supporting this, overall
293 relative proportions of phospholipids in C2C12 cells remained unchanged following PIK3C2B inhibition
294 unless PIK3C3 was depleted. A recent study demonstrated that MTM1 is essential for regulating
295 phosphoinositide metabolism in C2C12 cells, with a notable influence on PtdIns3P distribution and
296 turnover within endosomal compartments(34) and, similar to our own findings, terminal differentiation..
297 Depleting PIK3C2B in these cells restored PtdIns3P levels, corrected the trafficking defects and increased
298 terminal differentiation. Collectively, these findings suggest that lack of functional MTM1 triggers a
299 cascade of events that may disrupt the ability of activated satellite cell progeny (myoblasts) to fuse with
300 existing myofibers. This hypothesis aligns with the developmental timing of XLMTM manifestation in
301 both humans and experimental models, which coincides with a phase of rapid post-natal growth
302 dependent on satellite cells and potentially tertiary myoblast populations. (44, 57)

303 To identify potential early or dynamic markers of XLMTM, we compared the miRNA profiles of muscle
304 tissue from animals treated with, and subsequently withdrawn from, BLU3797. This analysis revealed a
305 distinct set of miRNAs whose expression levels changed in the disease state and normalized following
306 treatment. We observed increased *Srfp1* and *Smad1* transcript levels in XLMTM muscle, which
307 correlated with reduced levels of mir30a-3p/5p and mir26a-5p. Inhibition of PIK3C2B increased
308 mir30p/5p and mir26a-5p levels and ultimately decreased expression of SMAD1 and SFRP1 proteins.
309 Notably, these changes occurred alongside an opposite trend in myostatin levels, suggesting that the
310 regulation of these factors may become uncoupled in XLMTM, potentially contributing to disease
311 pathology.

Loss or inhibition of functional PIK3C2B is closely associated with normalization of disease markers and reduction in indicators of early muscle development or regeneration. To target this pathway, we developed BLU3797, a selective kinase inhibitor that specifically blocks PIK3C2B while sparing other lipid kinases. Using the *MTM1*$^{-/y}$ mouse model of human XLMTM, treatment with BLU3797 produced a dose-dependent improvement of disease symptoms, including rescue in survival and muscle function. Our data further show that altering dosing parameters directly influenced these outcomes. By testing BLU3797 as both a therapeutic intervention and a preventative of disease onset in mice, we demonstrated that our treatment window is broad and adaptable to a heterogenous disease and patient population. A limitation of our study is in the use of the wire hanging test to evaluate muscle function. Due to the complex behavior associated with wire hanging, and other factors that may influence test results (e.g., weight and balance), it is not always possible to relate the outcome of the test to a sole neuromuscular defect.

In summary, our findings demonstrate that selective inhibition of PIK3C2B, using compounds such as BLU3797, can normalize disease biomarkers, improve muscle function, and enhance survival in preclinical models of XLMTM. These results provide compelling evidence that targeting PIK3C2B may address key aspects of disease pathology, including the restoration of myoblast fusion and muscle regeneration. However, while the *MTM1*$^{-/y}$ mouse model offers valuable insights into the molecular mechanisms underlying XLMTM, it does not fully capture the complexity and heterogeneity of the disease as it manifests in humans. Therefore, further research in larger mammals, such as canine models and ultimately human subjects, is essential to validate the therapeutic potential of PIK3C2B inhibition. Continued investigation will be critical for advancing PIK3C2B inhibitors toward clinical application and for realizing their potential as part of the therapeutic strategy for XLMTM.

Methods

Sex as a biological variable

XLMTM is an X-linked genetic disorder, with the *MTM1* gene being present on the X chromosome and primarily affecting males. Phenotypes were compared between male and female WT and KO animals, and as expected, differences were observed between male and female animals. Experiments were therefore conducted in male animals with WT vs. *MTM1*$^{-/y}$ genotypes.

Generation of novel PIK3C2B small molecule inhibitors

BLU3797: (S)-N-(5-(2-(1-cyclopropylethyl)-7-(cyclopropylmethoxy)-1-oxoisoindolin-5-yl)-4-methylthiazol-2-yl)acetamide (Figure 1A; Supplemental Figure 7A)

Step 1: Synthesis of (S)-5-bromo-2-(1-cyclopropylethyl)-7-(cyclopropylmethoxy)isoindolin-1-one

To a solution of (S)-5-bromo-2-(1-cyclopropylethyl)-7-fluoroisoindolin-1-one (Intermediate 3, 100 mg, 0.335 mmol) and cyclopropylmethanol (121 mg, 1.68 mmol) in N,N-dimethylformamide (DMF; 1 mL) added Sodium tert-pentoxide (55.4 mg, 0.503 mmol) at 25°C and the mixture stirred at 110 °C for 1 h. The reaction mixture was concentrated under reduced pressure and the residue purified by prep-TLC (petroleum ether/Ethyl acetate) to furnish the titled compound as a white solid (100 mg, 85%). LCMS: *m/z* = 350 $[M+H]^+$;

Step 2: Synthesis of (S)-N-(5-(2-(1-cyclopropylethyl)-7-(cyclopropylmethoxy)-1-oxoisoindolin-5-yl)-4-methylthiazol-2-yl)acetamide

To a mixture of (S)-5-bromo-2-(1-cyclopropylethyl)-7-(cyclopropylmethoxy)isoindolin-1-one (Step 1, 40 mg, 0.114 mmol) and N-(4-methylthiazol-2-yl)acetamide (17.8 mg, 0.114 mmol) in DMF (2 mL) was added $Pd(OAc)_2$ (2.56 mg, 0.011 mmol) and Cs_2CO_3 (74.4 mg, 0.228 mmol) and tri-tert-

butylphosphonium tetrafluoroborate (6.63 mg, 0.023 mmol) at 25 °C and the reaction mixture stirred at 100 °C for 12 h under N_2. The reaction mixture was concentrated under reduced pressure and the residue was purified by *prep*-HPLC to furnish the titled compound as a brown solid (21.7 mg, 38%). LCMS: *m/z* = 426 $[M+H]^+$; ^{1}H NMR (400MHz, DMSO-d_6) δ: 7.22 (s, 1H), 7.03 (s, 1H), 4.65-4.52 (m, 2H), 4.05 (d, 2H), 3.72-3.61 (m, 1H), 2.44 (s, 3H), 2.24 (s, 3H), 1.39 (d, 4H), 1.20-1.10 (m, 1H), 0.72-0.62 (m, 3H), 0.51 (tt, 1H), 0.47-0.39 (m, 3H), 0.38-0.32 (m, 1H).

BLU2720: (S)-N-(5-(2-(1-cyclopropylethyl)-7-((1-methylazetidin-3-yl)methoxy)-1-oxoisoindolin-5-yl)-4-methylthiazol-2-yl)acetamide (Figure 1A; Supplemental Figure 7B)

Step 1: 5-bromo-2-[(1S)-1-cyclopropylethyl]-7-[(1-methylazetidin-3-yl)methoxy]isoindolin-1-one

To a solution of 5-bromo-2-[(1S)-1-cyclopropylethyl]-7-fluoro-isoindolin-1-one (100 mg, 335.40 umol, 1 *eq*) and (1-methylazetidin-3-yl)methanol (169.62 mg, 1.68 mmol, 5 *eq*) in DMF (1 mL) was added sodium;2-methylbutan-2-olate (55.41 mg, 503.10 µmol, 1.5 *eq*). The mixture was stirred at 110°C for 1 hr under N_2. LCMS showed desired MS. The reaction mixture was concentrated under reduced pressure and purified by *prep*-HPLC to afford 5-bromo-2-[(1S)-1-cyclopropylethyl]-7-[(1-methylazetidin-3-yl)methoxy]isoindolin-1-one as a yellow oil. (110 mg, 290.02 µmol, 86.47% yield) LCMS: *m/z* = 379.1 $[M+H]^+$

Step 2: N-[5-[2-[(1S)-1-cyclopropylethyl]-7-[(1-methylazetidin-3-yl)methoxy]-1-oxo-isoindolin-5-yl]-4-methyl-thiazol-2-yl]acetamide

To a solution of 5-bromo-2-[(1S)-1-cyclopropylethyl]-7-[(1-methylazetidin-3-yl)methoxy]isoindolin-1-one (30 mg, 79.10 umol, 1 *eq*) and N-(4-methylthiazol-2-yl)acetamide (13.59 mg, 87.00 umol, 1.1 *eq*) in DMF (1 mL) was added $Pd(OAc)_2$ (1.78 mg, 7.91 umol, 0.1 *eq*), Cs_2CO_3 (51.54 mg, 158.19 umol, 2 *eq*) and tritert-butylphosphonium;tetrafluoroborate (2.29 mg, 7.91 umol, 0.1 *eq*). The mixture was stirred

at 100°C for 12 hrs under N_2. The reaction mixture was concentrated under reduced pressure and purified by *prep*-HPLC to furnish N-[5-[2-[(1S)-1-cyclopropylethyl]-7-[(1-methylazetidin-3-yl)methoxy]-1-oxo-isoindolin-5-yl]-4-methyl-thiazol-2-yl]acetamide as a yellow solid. (8.2 mg, 15.32 µmol, 19.36% yield, 93.5% purity) LCMS: *m/z* = 455.1 $[M+H]^{+1}$; H-NMR (400 MHz, CD_3OD) δ ppm 8.55 (s, 1H), 7.31 (s, 1H), 7.08 (s, 1H), 4.73-4.55 (m, 2H), 4.38 (br s, 2H), 4.28-4.05 (m, 4H), 3.73-3.58 (m, 1H), 3.09 (br s, 1H), 2.85 (br s, 3H), 2.44 (s, 3H), 2.33-2.17 (m, 3H), 1.45-1.23 (m, 4H), 1.22-1.11 (m, 1H), 0.76-0.62 (m, 1H), 0.56-0.45 (m, 1H), 0.44-0.36 (m, 1H), 0.32 (td, 1H, *J* = 4.4, 9.2 Hz).

PIK3C2B biochemical assay

The potency of compounds against the *in vitro* enzymatic activity of human PIK3C2B was determined by ADP-Glo™ format (Promega, USA). The lipid kinase reaction was performed in 10 mM $MgCl_2$, 100 mM NaCl, 1 mM EGTA, 0.03% CHAPS, 2 mM DTT, and 50 mM HEPES, at pH 7.5.. To initiate the enzyme reaction, 120 nM of human PIK3C2B enzyme (Cat# PV3574l, Thermo Scientific, USA) and 2 mM ATP (Sigma Aldrich, USA) were preincubated with compounds at 2x final concentration for 10 minutes, followed by the addition of an equal volume of 300 nM lipid substrate phosphatidylinositol diC8 (Cat# P-0008, Echelon Biosciences, USA) to a final concentration of 60 nM PIK3C2B, 1 mM ATP, and 150 nM diC8.. ADP generated during the kinase reaction was resynthesized to ATP, which was determined as a luminescence signal in a coupled luciferase/luciferin reaction with an EnVision Multimode Plate reader (Revvity, USA). Data were normalized to background control (0.5% DMSO) and 100% inhibition controls (10 µM BGT-226), and the half-maximal inhibitory concentration (IC_{50}) calculated using a 4-parameter logistic equation.

Kinome selectivity score determination

The kinase selectivity of BLU3797 was determined at 3 µM using the KINOMEscan screening platform (Eurofins, Luxembourg)... The S(10) score is the ratio calculated from the number of non-mutant kinases bound by the test compound over the total number of non-mutant kinases at the testing concentration, where 10% residual activity is used as threshold.

Target engagement assay

The NanoBRET™ Target Engagement Assay was utilized to determine target engagement in live cells.. . Target protein was expressed as a fusion with NanoLuc® luciferase and the ability of a compound of interest to displace a fluorescent tracer was performed following the manufacturers (Promega, USA) instructions

. In this manuscript, we used the commercially available assays for: phosphatidylinositol-4,5-bisphosphate 3-kinase catalytic subunit alpha (PIK3CA), PIK3C3, and PIK3CD. PIK3C2B, PIK3CG, and PIK3C2G fusion vectors were obtained from Promega's Tailored R&D Solutions group, tracers were developed in-house.

C2C12 cells

C2C12 cells are a mouse myoblast cell line (Cat# CRL-1772, ATCC, USA), cultured in DMEM with 20% fetal bovine serum (FBS). *MTM1*-null clones were generated by genOway (France) through targeting of exon 5 with either insertion of a stop or indel sequence. WT or the resulting *MTM1*-null C2C12 cells were then transduced with either non-targeting shRNA (Cat# SCH016H, Millipore-sigma, USA) or PIK3C2B targeting shRNA (TRNC0000360889, CTTCATCATGGTGATGCATAT, Millipore-Sigma, USA) at an MOI of 1:10. Cells were then selected with 5 µg/ml puromycin (Cat# J67236.XF, ThermoFisher, USA) for 14 days and subsequently maintained at 2 µg/ml puromycin until time of assay.

C2C12 cells imaging assay

5000 cells/well were plated in a 96-well PhenoPlate (Revvity, USA). Cells were allowed to adhere and grow for 48 hours before growth media was replaced with differentiation media, DMEM with 2% horse serum (Invitrogen, USA). After 72 hours, media was replenished and compounds were added at the indicated concentrations. Cells were treated with compounds for 48 hours before a 15-minute fixation by addition of 4% paraformaldehyde in phosphate-buffered saline (PBS) with 4% sucrose to media. Cells were washed twice with Tris-buffered saline (TBS) and then permeabilized for 5 minutes with 0.1% TBS Triton X-100. After a TBS wash, cells were incubated with 10% neutral goat serum in TBS overnight at 4 °C, followed by an overnight incubation with primary anti-myosin antibody (Cat# MAB4470, MF20, R&D systems, USA) at a 1:1000 dilution. Cells were then washed 3 times with 0.05% TBS Tween-20 and incubated (1:1000) with Alexa-568 secondary antibody (Cat# A-21144, Invitrogen, USA) for 2 hours, after which they were counterstained with 1 µg/mL 4',6-diamidino 2-phenylindole (Invitrogen, USA) for 30 minutes. Cells were then washed 3 times with 0.05% TBS Tween-20, covered with 50% glycerol and covered with aluminum plate covers (Nunc, Denmark).

Plates were analyzed using an Opera Phenix Plus High-Content imager (Revvity, USA), all images were taken using the 20x confocal setting.. The number of nuclei within Alexa-568 positive objects was then quantified in addition to total positive area and number of individual objects.

C2C12 cell Mass Spectrometry

C2C12 were cultured in DMEM with 20% fetal bovine serum, harvested with 0.25% trypsin and snap-frozen as pellets containing 3 million cells. Cell pellets were resuspended in lysis buffer from the PreOmics iST-BCT® kit (PreOmics, Germany) and heated at 90 °C with shaking at 750 rpm for 10 min using an Eppendorf ThermoMixer® C to achieve cell lysis. Lysates were subsequently sonicated for 10

min (30 s on/30 s off) using a QSonica 700 Microplate Sonicator (Qsonica, USA) to shear DNA. . For each sample, 100 µg of protein was transferred to a 96-well Eppendorf Protein LoBind® PCR plate and adjusted to a final volume of 50 µL with BCT lysis buffer. Samples were digested overnight with trypsin at 37 °C with shaking at 750 rpm on an Eppendorf ThermoMixer® C. Peptide cleanup was performed using PreOmics BCT Phoenix cartridges according to the manufacturer's protocol (PreOmics, Germany). Eluted peptides were quantified for total protein , dried in a Savant SPD2030 SpeedVac (ThermoFisher, USA), and resuspended in 0.1% formic acid (MilliporeSigma, USA). For LC–MS/MS analysis, 600 ng of peptides per sample were injected onto an Evosep One system (Evosep, Denmark) coupled to a timsTOF-HT mass spectrometer (Bruker, USA), using a 40 SPD Whisper Zoom method and diaPASEF acquisition. Raw data were processed using DIA-NN (v1.8) in library-free, high-precision mode.

Mutant mouse strains

A *D1212A PIK3C2B*–constitutive mutant mouse model was generated at GenOway (France) by inserting GAT->GCC within exon 25 to create a PIK3C2B kinase-dead knock-in (KI) mouse in C57BL/6 genetic background (Supplemental Figure 1A). . Validated ES cell clones were injected into blastocysts to generate chimeric animals. Progeny were genotyped by PCR, forward: 5'-GCAAATCCAGACAGGAAGACCTTAGTGG-3' and reverse: 5'-CAGGAAGTGTGAAGCTGCCTCAGCT-3', to detect either a 254 base pair (bp) WT allele or a 345 bp KI allele. A subset of PCR-validated animals underwent further analysis by DNA sequencing to fully verify the integrity of the targeted region.

The *MTM1*-null mouse in a *129S5 x C57BL/6J-Tyr$^{c\text{-}Brd}$* background was acquired from Taconic (model# TF0892). Genotyping primers, forward: 5'- TCTCAGTGTTTAGGATTGAATCAGG-3', WT reverse: 5'-CCCAGGTGGTTCTAATGAGC-3' and KO reverse: 5'- ATAAACCCTCTTGCAGTTGCATC-3', were used to detect either the 280 bp WT allele or 241 bp KO allele.

The *MTM1* conditional KO mouse was generated at Mirimus (USA) by introducing loxP sequences upstream and downstream of exon 4 in pure C57BL/6N ES cells using CRISPR/Cas9 technology (Supplemental Figure 2A). Progeny were genotyped using PCR (forward: 5'- TTGTCAACCTACCACCCAGC-3' and reverse: 5'- GTAGACCAGAGCCAGAGCAC-3' to detect either the 155 bp WT allele or the 195 bp KI allele. A subset of PCR-validated animals underwent further analysis by DNA sequencing to fully verify the integrity of the targeted region. *Rosa26-CreER^{T2}* transgenic mice (B6.129-Gt(ROSA)26Sortm1(cre/ERT2)Tyj/J) (58) were acquired from Jackson Labs (stock number 008463).

Housing and husbandry

Mice included in this study were housed either at Charles River Laboratories (Lyon, France) or at Blueprint Medicine Corporation's animal care facility. Mice were housed in temperature and humidity-controlled rooms, with a 12:12 h light:dark cycle with 10-15 room air changes per hour. Animals were housed in disposable individually ventilated rodent cages (Innovive, USA) pre-filled with alpha-dri bedding (Innovive, USA) and a minimum of 2 enrichment devices. Animals not breeding were fed irradiated PicoLab® 5053 pelleted rodent chow (LabDiet, USA) and allowed access to acidified water, ad libitum. Breeding animals were fed irradiated PicoLab® 5058 chow (LabDiet, USA), 20% protein and 9% fat pelleted diet, and allowed access to acidified water, ad libitum.

Oral dosing of PIK3C2B inhibitors

Animals in the study were weaned on post-natal day 21 and given a combination of electrolyte gel (Bio-Serve, USA), transgenic dough diet (Bio-Serv, USA), and a small amount of irradiated PicoLab® 5058 pelleted diet (LabDiet, USA) containing 20% protein and 9% fat. Animals were enrolled in the study based on their date of birth. Weights were measured at the beginning of the study and before each dose administration. Formulations of BLU3797 were prepared immediately prior to dose administration. A

solution of 0.5% (w/v) of sodium carboxymethyl cellulose, 1% (v/v) Tween 80 in water was used as vehicle. Any animal found to be in a moribund state was removed from the study. Animal dosing was initiated on post-natal day 22 unless otherwise stated.

Terminal whole blood samples were collected via cardiac puncture. Muscle tissue (gastrocnemius and tibialis anterior) was snap frozen or harvested and fixed in 10% neutral buffered formalin for 48 hours before being placed in 70% ethanol prior to processing for histology or .

In vivo phenotypic studies

The TREAT-NMD Neuromuscular Network recommended wire hanging test for evaluating overall subacute muscle function and coordination in mice (SOP DMD_M.2.1.004) was utilized in this study. Motor coordination, grip strength, and muscle function were assessed by recording how long a mouse could hold onto an inverted wire cage top, up to a maximum of 60 seconds.. Mice were subjected to the MotoRater test (TSE systems, USA) at Charles River Laboratories (Finland) to assess fine-motor-kinematic analysis. Mice were acclimatized to the testing room for a minimum of 30 minutes before their walking motion was recorded by high-speed cameras (300 FPS) positioned above, below, and on either side of the animal. Videos of each mouse were then processed using Simi Motion software (Simi, Germany) and a custom-made automated analysis system was employed to analyze various gait patterns and movements (59-61).

Histological analysis

IHC staining of laminin in formalin-fixed, paraffin-embedded mouse gastrocnemius muscle was conducted on the Bond RX platform (Leica Biosystems, Germany) using standard chromogenic methods. Prior to staining, slides were incubated with Proteinase K for 5 minutes at room temperature followed by a 45-minute incubation with the Laminin antibody (Cat# ab11575, Abcam, UK). Antibody binding was

detected using a horseradish peroxidase-conjugated anti-rabbit secondary polymer and visualization was achieved through chromogenic staining with 3,3'-DAB. Nuclei were visualized using a hematoxylin counterstain. Sections were digitally scanned using an Aperio AT2 whole slide scanner (Leica Biosystems, Germany). Image analysis of the digital slide images was performed using the Oncotopix® Discovery software (Visiopharm, Denmark).

To determine the percentage of myocytes containing central nuclei, a manual counting method was employed. The entire muscle sample was thoroughly examined, and representative fields of view were selected based on notable myofiber changes. In each of the 5 high-powered fields (400x), 30 myocytes were counted to obtain accurate data.

To enhance the identification of myocytes, a deep-learning artificial intelligence (AI) algorithm was trained. The IHC stained slide was utilized to define a specific region of interest (ROI) that encompassed the cross-sectional muscle tissue. The AI algorithm processed these ROIs to accurately identify myocytes. The diameter of each identified myocyte was measured along its lesser diameter, providing additional quantitative information.

RNA analysis

Total RNA was obtained from tissues using the miRNeasy Tissue/Cells Advanced Micro Kit (cat# 217684, Qiagen, Germany) following the manufacturer's instructions. Isolated miRNAs were analyzed using the NanoString V1.5 miRNA kit (cat# 150649, NanoString, USA) and nCounter following the manufacturer's instructions. Relative miRNA levels and group comparisons were made using ROSALIND (Rosalind.bio, USA). qPCR analysis of miRNAs was performed using miRCURY LNA miRNA PCR assay kits (Qiagen, Germany). *Smad1*, *Sfrp1*, and glyceraldehyde 3-phosphate dehydrogenase (*Gapdh*) mRNA abundance

was assessed using TaqMan Probes (Thermo Fisher, USA) from complementary DNA generated using Superscript IV (Thermo Fisher, USA).

Detection of muscle PtdIns3P*, SQSTM1/P62, SFRP1, and plasma myostatin*

PtdIns3P was extracted from muscle using a lipid extraction kit (Abcam, UK). Briefly, gastrocnemius muscles were collected and snap-frozen in liquid nitrogen before being moved to a 2 mL microcentrifuge tube containing metal beads (Cayman Chemical, USA). 500 µl of lipid extraction buffer was added to the sample, mixed at room temperature for 15 minutes and homogenized in a Precellys 24 Touch instrument (Cayman Chemical, USA). Lysate was transferred to a clean microcentrifuge tube and spun at 10,000 g for 5 minutes. The supernatant was collected and dried using a vacuum drier. PtdIns3P was detected using a PtdIns3P mass enzyme-linked immunosorbent assay (ELISA; Echelon Biosciences, USA) according to the manufacturer's instructions.

To assess SQSTM1/P62 or SFRP1 levels, muscles were homogenized in RIPA buffer (cat# 889900, Thermo Fisher, USA), supplemented with cOmplete™ EDTA-free protease inhibitor cocktail, 50 mM sodium fluoride, 1 mM phenylmethanesulfonyl fluoride, 1 mM sodium orthovanadate, 2 mM β-glycerophosphate (all from Sigma-Millipore, USA), and HALT™ protease and phosphatase inhibitor cocktail (Thermo Fisher, USA). For SQSTM1/P62, homogenates were clarified and 5–20 µg of total protein was diluted in assay buffer and analyzed using a SQSTM1/P62 ELISA kit (Enzo Life Sciences, USA) following the manufacturer's instructions. SFRP1 was assessed in a similar fashion using the SFRP1 ELISA kit (Antibodies.com, UK). Myostatin levels were quantified from mouse plasma samples using the Quantikine Myostatin/GDF-8 ELISA kit (R&D Systems, USA) following the manufacturer's instructions.

Western blotting

Muscles were processed as above but denatured in loading buffer (Bio-Rad Laboratories, USA), run on TGX gels, and transferred using semi-dry transfer packs (Bio-Rad Laboratories, USA). Cells were harvested on ice using Phosphsafe extraction buffer (Millipore-Sigma, USA) with HALT protease-phosphatase inhibitors (Thermo Fisher, USA). Membranes were blocked and stained using LI-COR TBS blocking buffer and visualized using a LI-COR Odyssey (LI-COR Biotechnology, USA). Secondary antibodies goat anti-mouse 680 and goat anti-rabbit 800 were used at 1:5000. Primary antibodies: mouse-anti GAPDH (cat# 5174, Cell Signaling Technologies, USA), rabbit-anti SQSTM1/P62 (cat#5114, Cell Signaling Technologies, USA), rabbit-anti SMAD1 (cat#6944, Cell Signaling Technologies, USA), mouse anti-myosin heavy chain (Cat# MAB4470, MF20, R&D systems, USA), mouse anti-Myogenin (Cat# 15-5643-82, Thermo Fisher, USA), mouse anti-MyoD (Cat# MA1-41017, Thermo Fisher, USA), mouse anti-PAX7 (Cat# MAB1675, R&D Systems, USA), rabbit anti-actin (cat#8456, Cell Signaling Technologies, USA), mouse anti-PIK3C2B (Cat# 24788-1-AP, Protein Tech, USA), rabbit anti-MTM1 (PA5-17972, Thermo Scientific, USA) were all used at 1:1000 dilutions. Mouse anti-β actin (Cat# 3700, Cell Signaling Technologies, USA) was used at a 1:5000 dilution.

Proteomics/phosphoproteomics and lipidomics analysis

Analysis of tandem mass tag–labeled peptides to capture the proteome and phosphoproteome in *PIK3C2B*$^{+/+}$; *MTM1*$^{-/y}$ and *PIK3C2B*$^{D1212A/D1212A}$; *MTM1*$^{-/y}$ mouse muscles was performed using liquid chromatography with tandem mass spectrometry at IQ Proteomics (USA). For both readouts, UniProt Mouse (2018) was used for peptide assignment and a target-decoy strategy through weighted linear discriminant analysis was used to filter out false-positive peptides. Differential abundance was evaluated using empirical Bayes moderated *t*-tests (62) and adjusted for false discovery rate. Protein-protein interaction and pathway analysis of differentially abundant genes was performed using the STRING

database (63). Quantification of lipid molecules in *PIK3C3*$^{-/-}$ or *PIK3C3*$^{+/+}$ C2C12 cells treated with a PIK3C2B inhibitor or with DMSO was performed at Lipotype GmbH (Germany) with their Shotgun Lipidomics platform. Briefly, Orbitrap mass spectrometry with lipid class-specific internal standards provided absolute quantification of lipids. A proprietary software, LipotypeXplorer, using molecular fragmentation query language identified lipids in the mass spectra and further data processing and analysis was performed using the Lipotype library information and management system. Lipids were assigned to lipid classes for further analysis. Data were log transformed, and Z-scores scaled for differential abundance analysis using empirical Bayes moderated *t*-tests (62).

Statistics

Unless stated, descriptive statistics were done with either means, quartiles, and ranges (box-and-whisker plots) or means and standard errors of the mean. Comparison of myocyte fusion, number, and nuclei fraction in C2C12 cells were done by one-way analysis of variance (ANOVA) with Dunnett's correction for multiple comparisons. Comparisons of wire hanging latency, percentage of myofibers with central nuclei, myofiber diameter (in *MTM*$^{-/y}$/BLU3797 experiments), plasma myostatin, and myofiber nuclei density were done by Kruskal-Wallis test with Dunn's correction for multiple comparisons. Comparisons of kinematic gait analyses, muscle SQSTM1/P62 expression (across BLU3797 dose levels), plasma myostatin levels, and SFRP1 expression in KO vs. WT C2C12 cells were done by one-way ANOVA with Tukey's correction for multiple comparisons. Comparisons of myofiber diameter (in *MTM*$^{-/y}$/PIK3C2B kinase-dead experiments) and muscle PtdIns3P expression were done by one-way ANOVA with Holm-Šídák's correction for multiple comparisons. Comparisons of select miRNAs across BLU3797 dosing regiments were done by unpaired T-test. Comparison of muscle SQSTM1/P62 expression between *MTM1* WT and *MTM1*-null at varying BLU3797 treatment initiation timings were done by one-way ANOVA with Šídák's correction for multiple comparisons. P values less than 0.05 were considered significant.

Study approval

No studies involved human participants. All animal experiments were conducted in full compliance with local, national, ethical, and regulatory principles and local licensing regulations under approved Institutional Animal Care and Use Committee protocols following United States Department of Agriculture guidelines and regulations for research.

Data availability

The underlying data for the graphs is available in the Supporting Data Values file included as part of the supplementary material to this article.

Declarations

Consent for publication

Not applicable.

Competing interests

AS: Current employee of Blueprint Medicines Corporation, a wholly owned subsidiary of Sanofi.

MB: Current employee of Blueprint Medicines Corporation, a wholly owned subsidiary of Sanofi.

MC: Current employee of Blueprint Medicines Corporation, a wholly owned subsidiary of Sanofi.

TS: Current employee of Blueprint Medicines Corporation, a wholly owned subsidiary of Sanofi.

JH: Current employee of Blueprint Medicines Corporation, a wholly owned subsidiary of Sanofi.

GK: Current employee of Blueprint Medicines Corporation, a wholly owned subsidiary of Sanofi.

EP: Current employee of Blueprint Medicines Corporation, a wholly owned subsidiary of Sanofi.

JB: Current employee of Blueprint Medicines Corporation, a wholly owned subsidiary of Sanofi.

KF: Former employee of Blueprint Medicines Corporation, a wholly owned subsidiary of Sanofi.

SS: Former employee of Blueprint Medicines Corporation, a wholly owned subsidiary of Sanofi.

JCL: Current employee of Blueprint Medicines Corporation, a wholly owned subsidiary of Sanofi.

Funding

- This study was funded by Blueprint Medicines Corporation, a wholly owned subsidiary of Sanofi.

Authors' contributions

JCL, **SS**, and **KF** contributed to the original research ideas and evolution of overarching research goals and aims. **JCL**, **AS**, **MB**, and **JH** contributed to the development of methodology and creation of models. **MB**, **AS**, and **MC** contributed to the verification, whether as a part of the activity or separate, of the overall replication, reproducibility of results, experiments or other research outputs. **MB**, **AS**, and **MC** contribute to application of statistical, mathematical, computational, or other formal techniques to analyze or synthesize study data. **MB**, **TS**, **EP**, **AS**, **JH**, and **GK** contributed to conduction of the research and investigational processes, specifically performing the experiments, or data and evidence collection. **MB**, **TS**, **MC**, **EP**, **JB**, and **AS** contributed to the provision of study materials, reagents, laboratory samples, animals, instrumentation, computing resources, or other analysis tools. **MB**, **AS**, and **MC** contribute to management activities to annotate (produce metadata), scrub data and maintain research data for initial use and later reuse. **JCL** and **AS** contributed the preparation, creation, or presentation of the published work, specifically writing the initial draft. **MB**, **JCL**, **TS**, **AS**, **MC**, **JH**, **GK**, **EP**, **JB**, **KF**, and **SS** contributed to the preparation, creation, or presentation of the published work by those from the original research group, specifically critical review, commentary, or revision—including at pre- or post-publication stages.

MB, **JCL**, **AS**, and **JH** contributed to the preparation, creation, or presentation of the published work, specifically visualization and data presentation. **JCL**, **TS**, **SS**, and **KF** contributed to the oversight and leadership responsibility for the research activity planning and execution, including mentorship external to the core team. **MB**, **TS**, **JCL**, and **AS** contributed to the management and coordination responsibility for the research activity planning and execution.

Acknowledgements

The authors extend their gratitude to the many colleagues at Blueprint Medicines, a Sanofi company, whose efforts were instrumental in enabling this work. We thank A. Garner and K. Hoeflich for providing input for the initial validation, C. Petrino for her contributions to the microRNA work, A. Ozen for her contributions to building the binding site model, and F. Scheuplein, S. Ribich, and P. Carter for their insightful discussions. The medical writing support was provided by Ashley Knox, PhD, and editorial support was provided by Travis Taylor, BA, all of Paragon (a division of Prime, Knutsford, UK) supported by Blueprint Medicines Corporation, a wholly-owned subsidiary of Sanofi.. Blueprint Medicines Corporation, a wholly-owned subsidiary of Sanofi, follows all current policies established by the International Committee of Medical Journal Editors and Good Publication Practice guidelines (link).

References

1. Jungbluth H, et al. Centronuclear (myotubular) myopathy. *Orphanet J Rare Dis.* 2008;3:26.
2. Tsai TC, et al. Characterization of MTM1 mutations in 31 Japanese families with myotubular myopathy, including a patient carrying 240 kb deletion in Xq28 without male hypogenitalism. *Neuromuscul Disord.* 2005;15(3):245-252.
3. Reumers SFI, et al. Clinical, genetic, and histological features of centronuclear myopathy in the Netherlands. *Clin Genet.* 2021;100(6):692-702.
4. Annoussamy M, et al. X-linked myotubular myopathy: A prospective international natural history study. *Neurology.* 2019;92(16):e1852-e1867.
5. Beggs AH, et al. A multicenter, retrospective medical record review of X-linked myotubular myopathy: The recensus study. *Muscle Nerve.* 2018;57(4):550-560.
6. Amburgey K, et al. A natural history study of X-linked myotubular myopathy. *Neurology.* 2017;89(13):1355-1364.
7. Bouma S, et al. Respiratory features of centronuclear myopathy in the Netherlands. *Neuromuscul Disord.* 2023;33(7):580-588.
8. Lawlor MW, Dowling JJ. X-linked myotubular myopathy. *Neuromuscul Disord.* 2021;31:1004-1012.
9. Molera C, et al. Intrahepatic cholestasis is a clinically significant feature associated with natural history of X-Linked Myotubular Myopathy (XLMTM): A case series and biopsy report. *J Neuromuscul Dis.* 2022;9(1):73-82.
10. Herman GE, et al. Medical complications in long-term survivors with X-linked myotubular myopathy. *J Pediatr.* 1999;134(2):206-214.
11. Lloyd A, et al. Estimation of the quality-of-life impact of X-linked myotubular myopathy. *J Neuromuscul Dis.* 2021;8(6):1047-1061.

12. Biancalana V, et al. Characterisation of mutations in 77 patients with X-linked myotubular myopathy, including a family with a very mild phenotype. *Hum Genet.* 2003;112(2):135-142.
13. Buj-Bello A, et al. Identification of novel mutations in the MTM1 gene causing severe and mild forms of X-linked myotubular myopathy. *Hum Mutat.* 1999;14(4):320-325.
14. Herman GE, et al. Characterization of mutations in fifty North American patients with X-linked myotubular myopathy. *Human Mutat.* 2002;19.
15. Laporte J, et al. MTM1 mutations in X-linked myotubular myopathy. *Hum Mutat.* 2000;15(5):393-409.
16. Jungbluth H, Gautel M. Pathogenic mechanisms in centronuclear myopathies. *Front Aging Neurosci.* 2014;6:339.
17. Leiden Open-source Variation Database (LOVD). The MTM1 gene homepage. https://databases.lovd.nl/shared/genes/MTM1. Updated October 29, 2024. Accessed February 13, 2025.
18. Fokkema IF, et al. LOVD v.2.0: The next generation in gene variant databases. *Hum Mutat.* 2011;32(5):557-563.
19. Bhattacharyya T, et al. Structural rationale to understand the effect of disease-associated mutations on Myotubularin. *Curr Res Struct Biol.* 2023;5:100100.
20. Laporte J, et al. The myotubularin family: from genetic disease to phosphoinositide metabolism. *Trends Genet.* 2001;17(4):221-228.
21. Oliveira J, et al. Expanding the MTM1 mutational spectrum: novel variants including the first multi-exonic duplication and development of a locus-specific database. *Eur J Hum Genet.* 2013;21(5):540-549.
22. Cowling BS, et al. Defective membrane remodeling in neuromuscular diseases: insights from animal models. *PLoS Genet.* 2012;8(4):e1002595.

23. Jang W, et al. Endosomal lipid signaling reshapes the endoplasmic reticulum to control mitochondrial function. *Science.* 2022;378(6625):eabq5209.
24. Tsujita K, et al. Myotubularin regulates the function of the late endosome through the gram domain-phosphatidylinositol 3,5-bisphosphate interaction. *J Biol Chem.* 2004;279(14):13817-13824.
25. Taylor GS, et al. Myotubularin, a protein tyrosine phosphatase mutated in myotubular myopathy, dephosphorylates the lipid second messenger, phosphatidylinositol 3-phosphate. *Proc Natl Acad Sci U S A.* 2000;97(16):8910-8915.
26. Lawlor MW, et al. Myotubularin-deficient myoblasts display increased apoptosis, delayed proliferation, and poor cell engraftment. *Am J Pathol.* 2012;181(3):961-968.
27. Fetalvero KM, et al. Defective autophagy and mTORC1 signaling in myotubularin null mice. *Mol Cell Biol.* 2013;33(1):98-110.
28. Pierson CR, et al. Modeling the human MTM1 p.R69C mutation in murine Mtm1 results in exon 4 skipping and a less severe myotubular myopathy phenotype. *Hum Mol Genet.* 2012;21(4):811-825.
29. Al-Qusairi L, et al. Lack of myotubularin (MTM1) leads to muscle hypotrophy through unbalanced regulation of the autophagy and ubiquitin-proteasome pathways. *FASEB J.* 2013;27(8):3384-3394.
30. Dowling JJ, et al. Loss of myotubularin function results in T-tubule disorganization in zebrafish and human myotubular myopathy. *PLoS Genet.* 2009;5(2):e1000372.
31. Sabha N, et al. PIK3C2B inhibition improves function and prolongs survival in myotubular myopathy animal models. *J Clin Invest.* 2016;126(9):3613-3625.
32. Gulluni F, et al. Class II PI3K Functions in Cell Biology and Disease. *Trends Cell Biol.* 2019;29(4):339-359.

33. Massana-Munoz X, et al. Inactivating the lipid kinase activity of PI3KC2beta is sufficient to rescue myotubular myopathy in mice. *JCI Insight.* 2023;8(9).
34. Mansat M, et al. PI3KC2β depletion rescues endosomal trafficking defects in Mtm1 knockout skeletal muscle cells. *J Lipid Res.* 2025;66(3):100756.
35. Samso P, et al. Antagonistic control of active surface integrins by myotubularin and phosphatidylinositol 3-kinase C2beta in a myotubular myopathy model. *Proc Natl Acad Sci U S A.* 2022;119(40):e2202236119.
36. Mansat M, et al. MTM1-mediated production of phosphatidylinositol 5-phosphate fuels the formation of podosome-like protrusions regulating myoblast fusion. *Proceedings of the National Academy of Sciences.* 2024;121(23):e2217971121.
37. Koch C, et al. Myostatin: a Circulating Biomarker Correlating with Disease in Myotubular Myopathy Mice and Patients. *Mol Ther Methods Clin Dev.* 2020;17:1178-1189.
38. Katsuragi Y, et al. p62/SQSTM1 functions as a signaling hub and an autophagy adaptor. *The FEBS Journal.* 2015;282(24):4672-4678.
39. Bizieff A, et al. Changes in protein fluxes in skeletal muscle during sequential stages of muscle regeneration after acute injury in male mice. *Scientific Reports.* 2024;14(1):13172.
40. Sun H, et al. Proteomic studies of rat tibialis anterior muscle during postnatal growth and development. *Mol Cell Biochem.* 2009;332(1-2):161-171.
41. Gerlach Melhedegaard E, et al. Myosin inhibition partially rescues the myofiber proteome in X-linked myotubular myopathy. *JCI Insight.* 2025;10(24).
42. Coley WD, et al. Effect of genetic background on the dystrophic phenotype in mdx mice. *Hum Mol Genet.* 2016;25(1):130-145.
43. Bachman JF, et al. Prepubertal skeletal muscle growth requires Pax7-expressing satellite cell-derived myonuclear contribution. *Development.* 2018;145(20).

44. White RB, et al. Dynamics of muscle fibre growth during postnatal mouse development. *BMC Dev Biol.* 2010;10:21.
45. Cramer AAW, et al. Nuclear numbers in syncytial muscle fibers promote size but limit the development of larger myonuclear domains. *Nat Commun.* 2020;11(1):6287.
46. Doetschman T. Influence of genetic background on genetically engineered mouse phenotypes. *Methods Mol Biol.* 2009;530:423-433.
47. Zhang BW, et al. miR-30-5p regulates muscle differentiation and alternative splicing of muscle-related genes by targeting MBNL. *Int J Mol Sci.* 2016;17(2):182.
48. Dey BK, et al. miR-26a is required for skeletal muscle differentiation and regeneration in mice. *Genes Dev.* 2012;26(19):2180-2191.
49. Chen B, et al. Circular RNA circHIPK3 promotes the proliferation and differentiation of chicken myoblast cells by sponging miR-30a-3p. *Cells.* 2019;8(2):177.
50. Liu Y, et al. miR-324-5p inhibits C2C12 cell differentiation and promotes intramuscular lipid deposition through lncDUM and PM20D1. *Mol Ther Nucleic Acids.* 2020;22:722-732.
51. Li H, et al. circFGFR4 promotes differentiation of myoblasts via binding miR-107 to relieve its inhibition of Wnt3a. *Mol Ther Nucleic Acids.* 2018;11:272-283.
52. Odame E, et al. miR-145-3p inhibits MuSCs proliferation and mitochondria mass via targeting MYBL1 in Jianzhou big-eared goats. *Int J Mol Sci.* 2023;24(9):8341.
53. Svensson A, et al. Secreted frizzled related protein 1 (Sfrp1) and Wnt signaling in innervated and denervated skeletal muscle. *J Mol Histol.* 2008;39(3):329-337.
54. Descamps S, et al. Inhibition of myoblast differentiation by Sfrp1 and Sfrp2. *Cell Tissue Res.* 2008;332(2):299-306.
55. Liu HP, et al. MiR-30a-3p promotes ovariectomy-induced osteoporosis in rats via targeting SFRP1. *Eur Rev Med Pharmacol Sci.* 2019;23(22):9754-9760.

56. Nojima J, et al. Dual roles of smad proteins in the conversion from myoblasts to osteoblastic cells by bone morphogenetic proteins. *J Biol Chem.* 2010;285(20):15577-15586.
57. Gattazzo F, et al. Distinct Phases of Postnatal Skeletal Muscle Growth Govern the Progressive Establishment of Muscle Stem Cell Quiescence. *Stem Cell Reports.* 2020;15(3):597-611.
58. Ventura A, et al. Restoration of p53 function leads to tumour regression in vivo. *Nature.* 2007;445(7128):661-665.
59. Heikkinen T, et al. Rapid and robust patterns of spontaneous locomotor deficits in mouse models of Huntington's disease. *PLoS One.* 2020;15(12):e0243052.
60. Preisig DF, et al. High-speed video gait analysis reveals early and characteristic locomotor phenotypes in mouse models of neurodegenerative movement disorders. *Behav Brain Res.* 2016;311:340-353.
61. Yavas A, et al. Detailed genetic and functional analysis of the hDMDdel52/mdx mouse model. *PLoS One.* 2020;15(12):e0244215.
62. Ritchie ME, et al. limma powers differential expression analyses for RNA-sequencing and microarray studies. *Nucleic Acids Res.* 2015;43(7):e47.
63. Szklarczyk D, et al. The STRING database in 2023: protein-protein association networks and functional enrichment analyses for any sequenced genome of interest. *Nucleic Acids Res.* 2023;51(D1):D638-D646.

Table 1. NanoBRET™-based determination of BLU3797and BLU2720 PI3K engagement.

IC_{50} (nM)	PIK3C2B	PIK3CA	PIK3C3	PIK3CG	PIK3CD	PIK3C2G
BLU3797	68.2	20,000	14,366	7233	12,364	6759
BLU2720	7297	20,000	20,000	20,000	13,806	20,000

IC_{50}, half-maximal inhibitory concentration; PIK3C2G, phosphatidylinositol-4-phosphate 3-kinase catalytic subunit type 2 gamma; PIK3C3, phosphatidylinositol 3-kinase catalytic subunit type 3; PIK3CA, phosphatidylinositol-4,5-bisphosphate 3-kinase catalytic subunit alpha; PIK3CD, phosphatidylinositol-4,5-bisphosphate 3-kinase catalytic subunit delta; PIK3CG, phosphatidylinositol-4,5-bisphosphate 3-kinase catalytic subunit gamma.

Figures

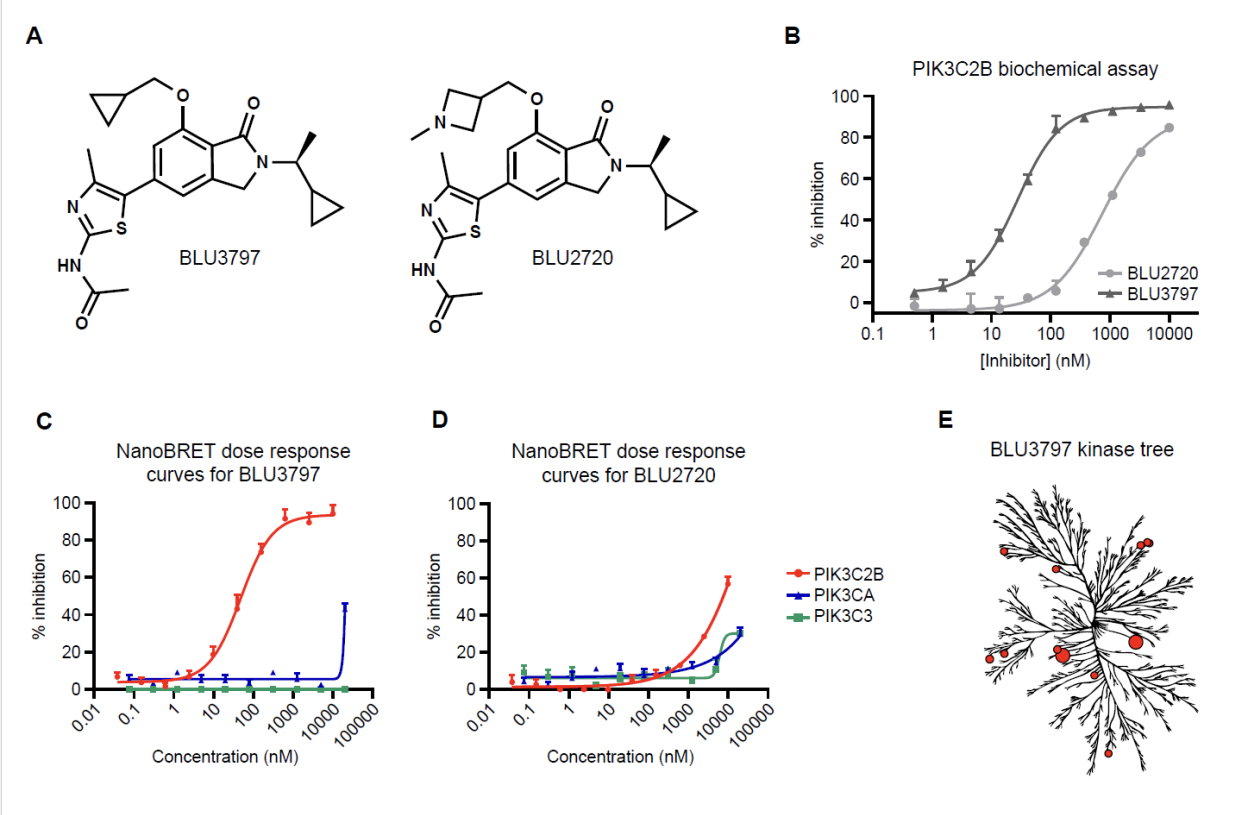

Figure 1. BLU3797 is a selective and potent inhibitor of human PIK3C2B kinase. (**A**) Chemical structures of BLU3797 and BLU 2720. (**B**) Biochemical analysis of PIK3C2B inhibitory activity of BLU3797 (IC_{50} = 28 nM) and BLU2720 (IC_{50} = 1.0 µM) in the presence of 1 mM ATP. (**C,D**) NanoBRET™-based determination of BLU3797and BLU2720 PI3K engagement. Individual points are mean ± SEM. (**E**) Kinome tree representing the reactivity of BLU3797 to other kinases as assessed by KINOMEscan (Eurofins, Luxembourg). Red dots represent kinases with significant BLU3797 interaction, dot size is proportional affinity. The S(10) of BLU3797 is 0.015, indicating high selectivity.
IC_{50}, half-maximal inhibitory concentration; PIK3C2B, phosphatidylinositol-4-phosphate 3-kinase catalytic subunit type 2 beta; PIK3C3, phosphatidylinositol 3-kinase catalytic subunit type 3; PIK3CA, phosphatidylinositol-4,5-bisphosphate 3-kinase catalytic subunit alpha; SEM, standard error of the mean.

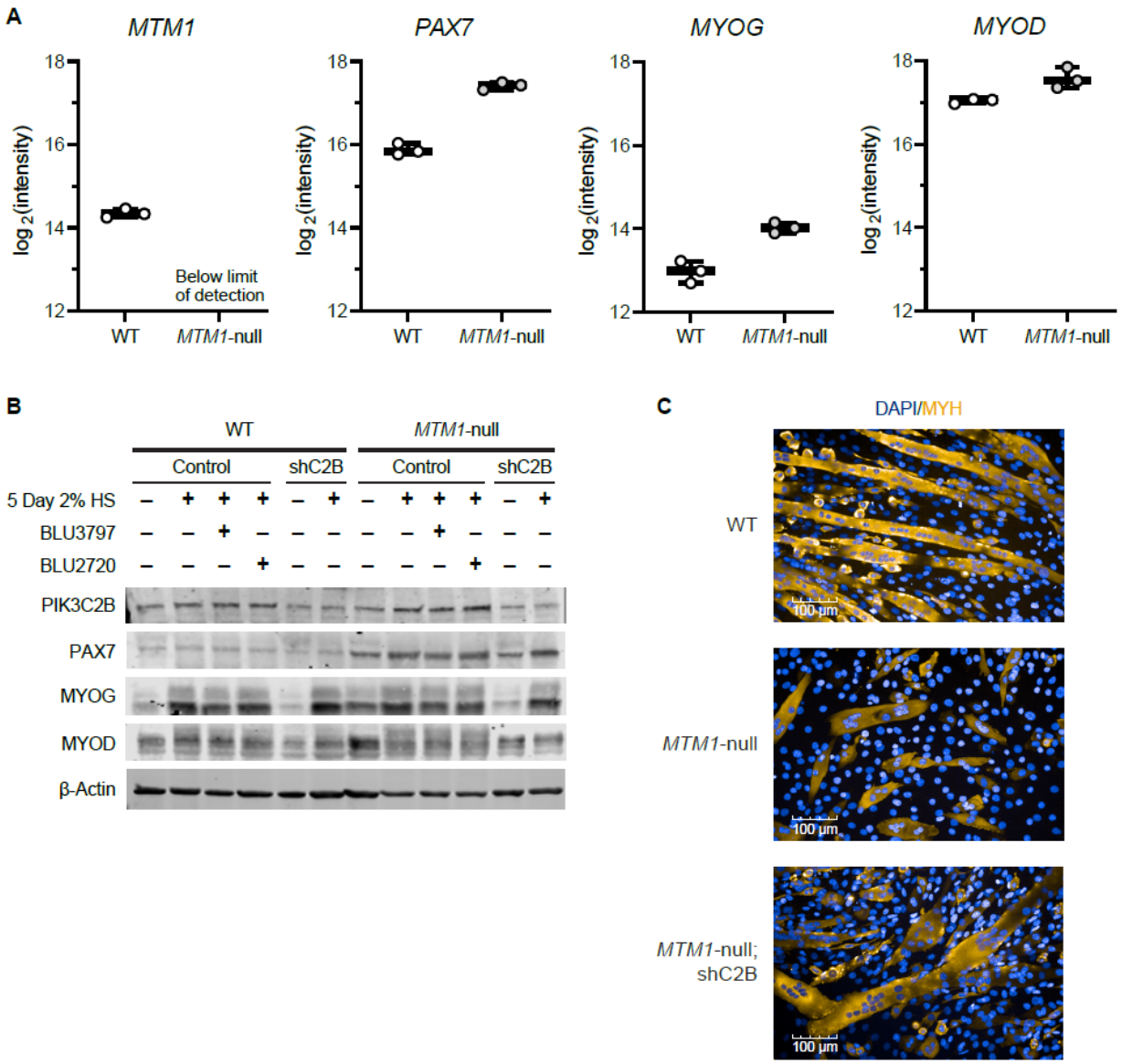

Figure 2. PIK3C2B depletion or inhibition does not negatively impact differentiation of C2C12 cells (**A**) Mass-spectrometry analysis of C2C12-cell lysates displaying raw-intensity values for selected genes. **(B)** Western blot of WT or *MTM1*-null C2C12 lysates, with or without PIK3C2B depletion (shC2B), harvested before or after differentiation (5 days 2% HS), compound treatment (500 nM) occurred during the last 48 hours of differentiation. **(C)** Example of cultures 5 days post differentiation stained for MYH (experiment conducted twice).

DAPI, 4',6-diamidino 2-phenylindole; MTM1, myotubularin 1; PAX7, paired box 7; MYOG, myogenin; MYOD, myogenic differentiation 1; MYH, myosin heavy chain; PIK3C2B, phosphatidylinositol-4-phosphate 3-kinase catalytic subunit type 2 beta; WT, wild-type.

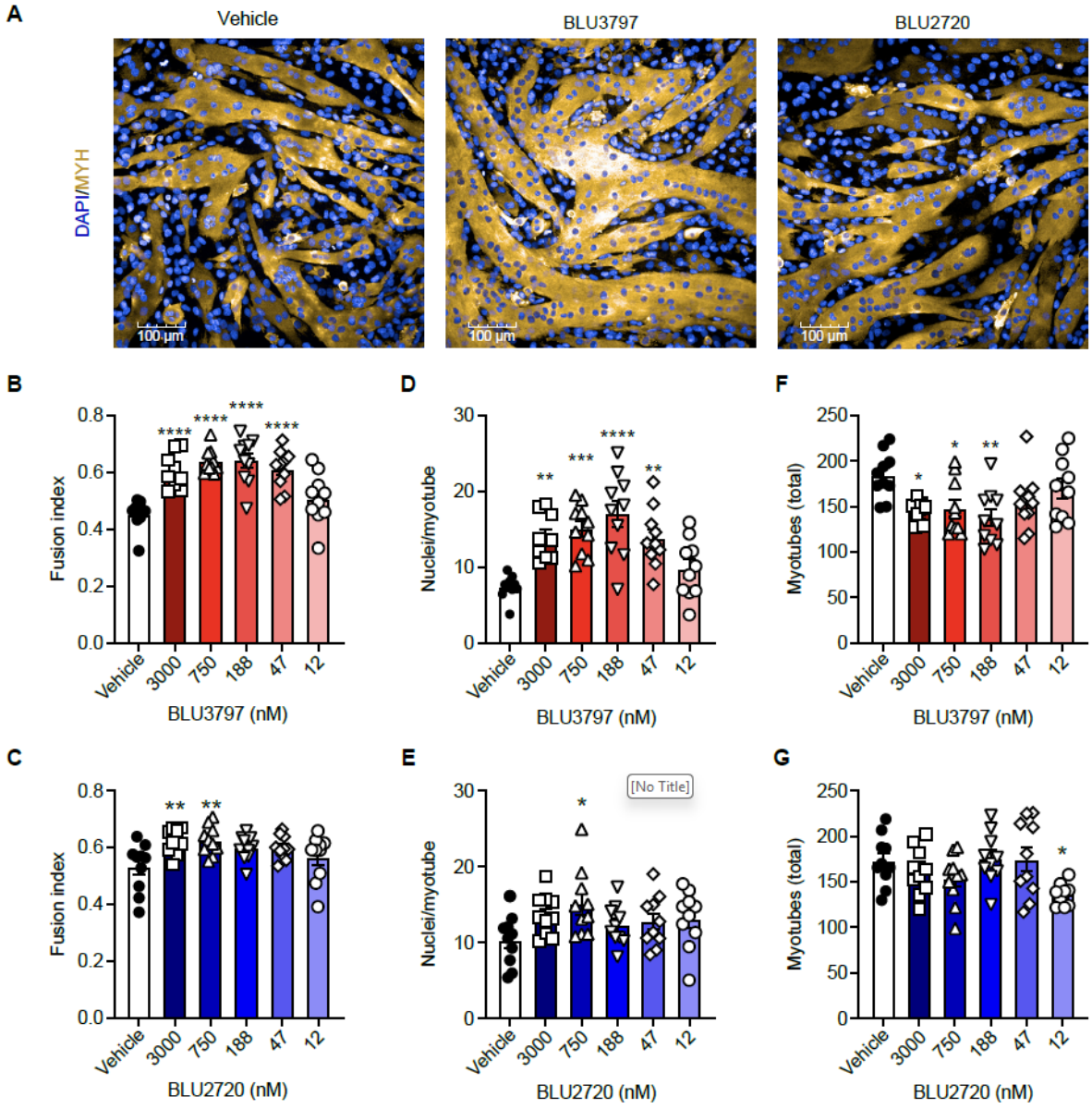

Figure 3. PIK3C2B inhibition promotes myocyte-myotube fusion in C2C12 cells. (**A**) Example images of *MTM1*-null C2C12 cells fixed after 5 days of differentiation (2% HS) and 3 µM of BLU3797 or BLU2720 treatment for the final 48 hours (experiment conducted 4 times). (**B**, **C**) Representative quantification (3 independent experiments) of the fraction of nuclei in MYH positive structures (Fusion Index) from 5 random non-overlapping fields (n = 10). (**D**, **E**) Representative quantification (3 independent experiments) of average nuclei in MYH positive structures (myotubes) from 5 random non-overlapping fields (n = 10). (**F**, **G**) Representative quantification of the total MYH positive structures (myotubes) from 5 random non-overlapping fields (n = 10). Error bars show SEM. *p≤0.05, **p≤0.01, ***p≤0.001, ****p≤0.0001. Comparisons were done by one-way analysis of variance (ANOVA) with Dunnett's correction for multiple comparisons.

API, 4’,6-diamidino 2-phenylindole; MTM1, myotubularin 1; MYH, myosin heavy chain; PIK3C2B, phosphatidylinositol-4-phosphate 3-kinase catalytic subunit type 2 beta; SEM, standard error of the mean.

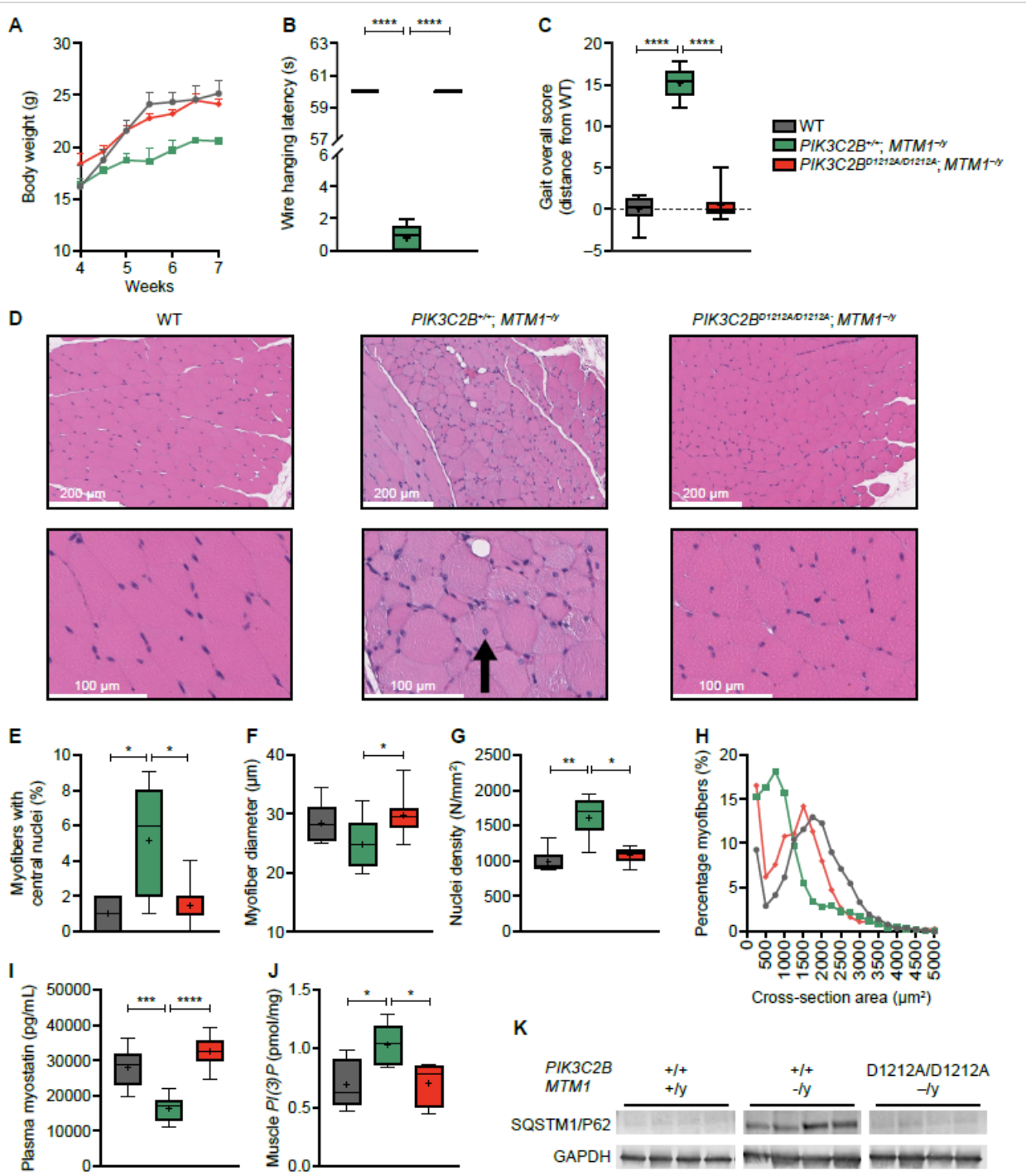

Figure 4. In a mouse model of XLMTM (*MTM1*$^{-/y}$), the presence of the PIK3C2B kinase dead mutation leads to the restoration of muscle function and histology. (**A**) Comparison of male *MTM1*$^{-/y}$, WT, and PIK3C2B kinase dead (PIK3C2B$^{D1212A/D1212A}$) *MTM1*$^{-/y}$ weight gain. (**B**) Analysis of muscle strength between by wire hanging latency. (**C**) Comparison of mobility and muscle coordination by kinematic-gait analysis. (**D**) Representative images of H&E-stained gastrocnemius muscle (experiment conducted 3 times). Arrow indicates myofiber with central nucleus. (**E**) Summary of histological analysis comparing percentage of

myofibers with centralized nuclei. (**F**) Summary of histological analysis examining myofiber diameter. (**G**) Summary of histological analysis of nuclear density within a tissue section. (**H**) Histogram profile of the cross-sectional area of myofibers. (**I**) Plasma myostatin level comparison. (**J**) Muscle PtdIns3P level comparison. (**K**) Western blot staining of SQSTM1/P62 from muscle lysates. Error bars show SEM. In box-and-whisker plots, median (line), mean (symbol), 25-75th quartile range (box), and minimum and maximum (whiskers) are shown. Number of animals per group ranged from 5 (*PIK3C2B*$^{+/+}$*MTM1*$^{-/y}$) to 10 (WT and *PIK3C2B*$^{-/-}$*MTM1*$^{-/y}$). *p < 0.05; **p < 0.01; ***p < 0.001; ****p < 0.0001. Comparisons of wire hanging latency, percentage of myofibers with central nuclei, myofiber diameter, plasma myostatin, and myofiber nuclei density were done by Kruskal-Wallis test with Dunn's correction for multiple comparisons. Comparisons of kinematic gait analyses were done by one-way ANOVA with Tukey's correction for multiple comparisons. Comparisons of myofiber diameter and muscle PtdIns3P expression were done by one-way ANOVA with Holm-Šídák's correction for multiple comparisons.
GAPDH, glyceraldehyde-3-phosphate dehydrogenase; H&E, hematoxylin and eosin; PIK3C2B, phosphatidylinositol-4-phosphate 3-kinase catalytic subunit type 2 beta; PtdIns3P, phosphatidylinositol 3-phosphate; MTM1, myotubularin 1; SEM, standard error of the mean; WT, wild-type; XLMTM, X-linked myotubular myopathy.

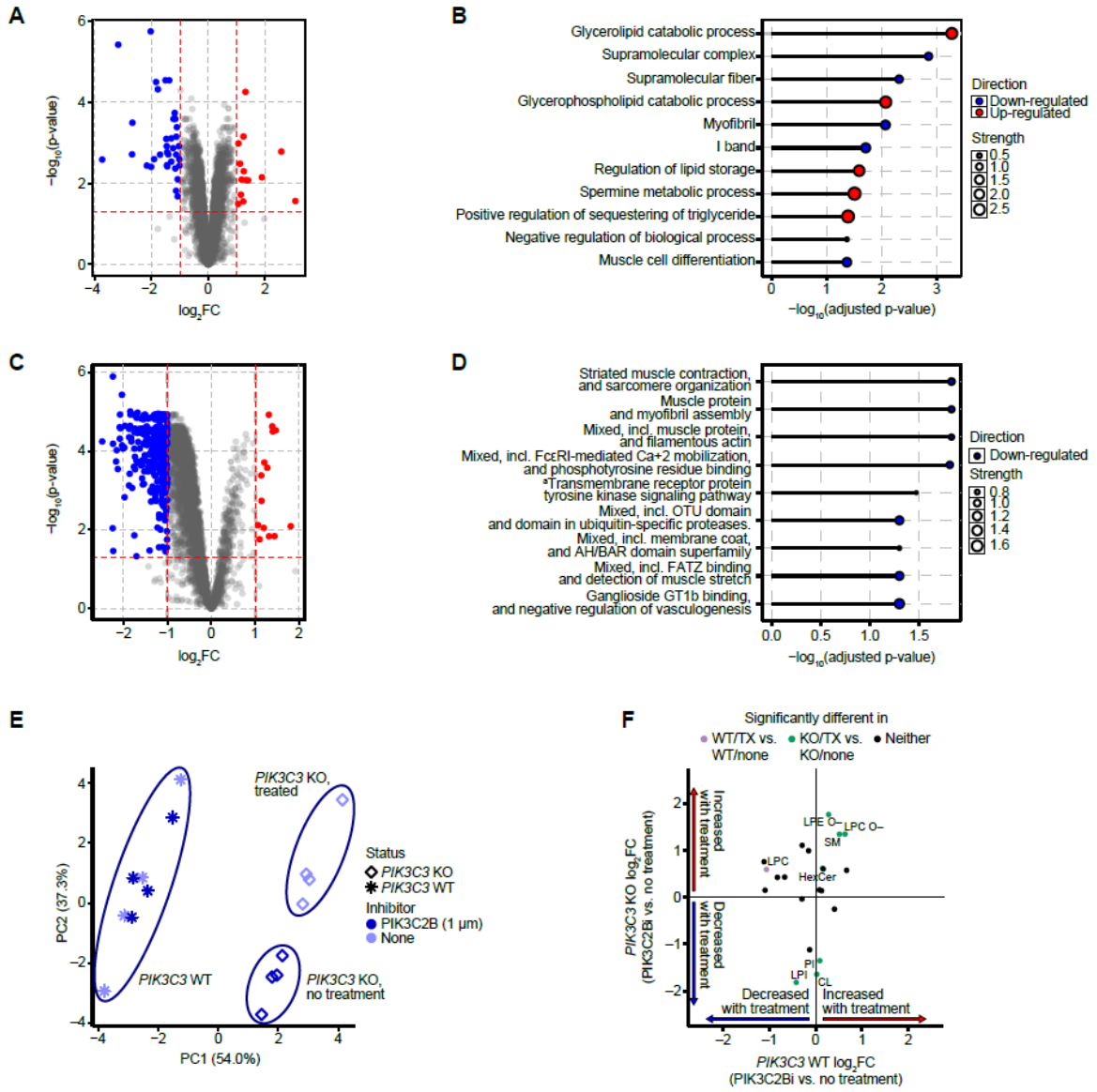

Figure 5. Proteomics and phosphoproteomics reveal decreases in abundance of muscle-related proteins in PIK3C2B kinase dead *MTM1* KO mice compared with *PIK3C2B* intact *MTM1* KO mice. (**A**) Differential proteome abundance in *MTM1*$^{-/y}$/*PIK3C2B*$^{D1212A/D1212A}$ mice (n=6) compared with *MTM1*$^{-/y}$/*PIK3C2B*$^{+/+}$ mice (n=5). (**B**) Significantly enriched (adjusted p < 0.05) GO pathways in the proteome of *MTM*$^{-/y}$/*PIK3C2B*$^{D1212A/D1212A}$ mice. (**C**) Differential phosphoproteome abundance in *MTM1*$^{-/y}$/*PIK3C2B*$^{D1212A/D1212A}$ mice compared with *MTM1*$^{-/y}$/*PIK3C2B*$^{+/+}$ mice. (**D**) Significantly enriched (adjusted p < 0.05) GO pathways in the phosphoproteome of *MTM*$^{-/y}$ /*PIK3C2B*$^{D1212A/D1212A}$ mice. [a]Transmembrane receptor protein tyrosine kinase signaling pathway, including FcεRI mediated Ca2+ mobilization. (**E**) Principal component analysis of *PIK3C3* KO and *PIK3C3* WT C2C12 cells that were treated with PIK3C2B inhibitor (1 µM) or not treated (n=4/group). (**F**) Congruence between fold change differences in *PIK3C3* KO/BLU3797 (1 µM) treated cells vs. *PIK3C3* KO cells without treatment and *PIK3C3* WT/PIK3C2B

inhibitor (1 µM) treated cells vs. *PIK3C3* WT cells without treatment. Comparison of lipid abundance profiles were done by Bayes-moderated t-tests. Significance assessed at $p < 0.05$.

GO, gene ontology; KO, knock-out; MTM1, myotubularin 1; PIK3C2B, phosphatidylinositol-4-phosphate 3-kinase catalytic subunit type 2 beta; PIK3C2Bi, phosphatidylinositol-4-phosphate 3-kinase catalytic subunit type 2 beta inhibitor, PIK3C3, phosphatidylinositol 3-kinase catalytic subunit type 3; WT, wild-type.

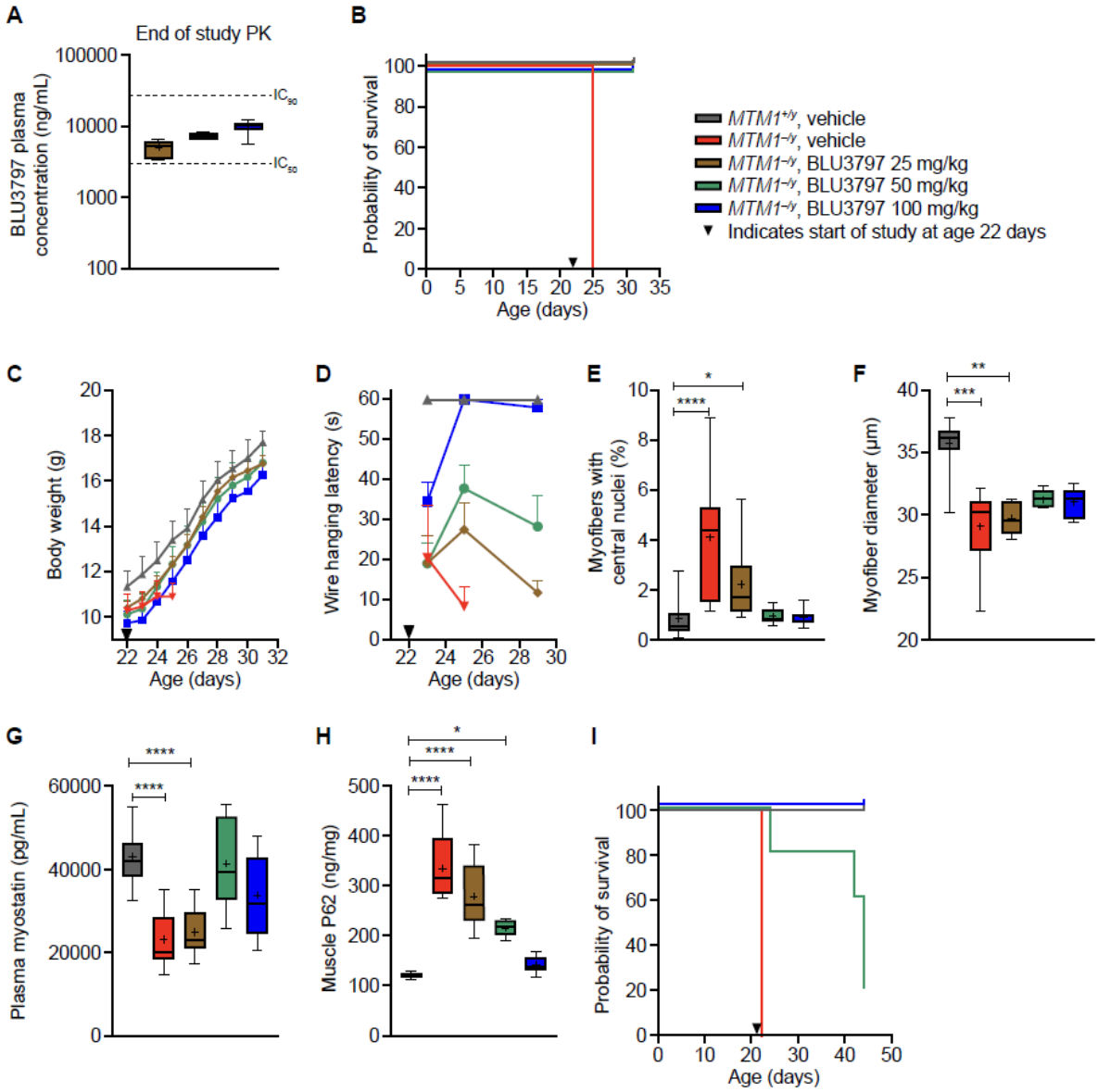

Figure 6. BLU3797 extends the lifespan of *MTM1*$^{-/y}$ male mice, reinstates muscle function, and improves histological characteristics. (**A**) 10-day study of plasma pharmacokinetics of BLU3797, administered orally once daily at 22 days of age, FBS-corrected NanoBRET™ IC_{50} and IC_{90} values are indicated. (**B**) Kaplan–Meier survival curve, *MTM1*$^{-/y}$ vehicle control group reached humane endpoints 3 days after the study start date. (**C**) Body weight. (**D**) Assessment of muscle strength by wire hanging latency. (**E**) Summary of histological analysis of muscle samples examining the percent of myofibers with centralized nuclei and the (**F**) myofiber diameter. (**G**) Plasma myostatin levels and (**H**) muscle SQSTM1/P62 levels (both detected by ELISA). (**I**) Kaplan–Meier survival curve for an extended 28-day study, Q48h, *MTM1*$^{-/y}$ vehicle control group reached humane endpoints 3 days after the study start date. Arrowheads represent start of study. Error bars show SEM. In box-and-whisker plots, median (line), mean (symbol), 25-75th quartile range (box), and minimum and maximum (whiskers) are shown. The number of

894 animals per group ranged from 5 to 7. *p < 0.05; **p < 0.01; ***p < 0.001; ****p < 0.0001.
895 Comparisons of wire hanging latency, percentage of myofibers with central nuclei, myofiber diameter,
896 plasma myostatin, and myofiber nuclei density were done by Kruskal-Wallis test with Dunn's correction
897 for multiple comparisons.
898 FBS, fetal bovine serum; IC_{50}, half-maximal inhibitory concentration; IC_{90}, 90% inhibitory concentration;
899 MTM1, myotubularin 1; PK, pharmacokinetics; Q48h, once every 48 hours; SEM, standard error of the
900 mean.

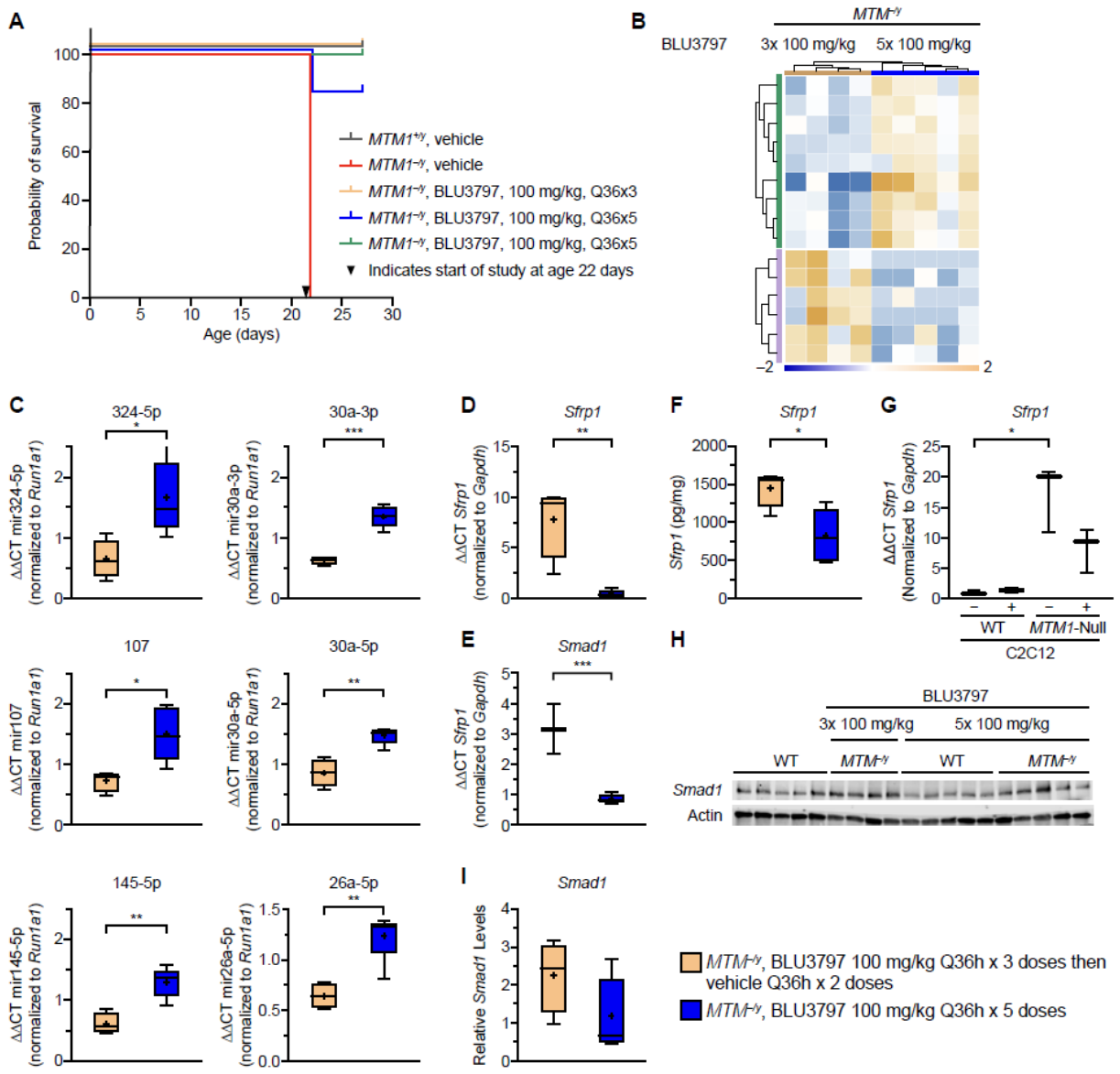

Figure 7. PIK3C2B inhibition alters miRNA expression and decreases muscle SFRP1 protein levels. (**A**) Survival of *MTM1*$^{-/y}$ mice treated with BLU3797 at the indicated number of times following a Q36h dosing schedule. Arrowhead represents start of the study. (**B**) Clustering of treatment groups by differential miRNA expression. (**C**) Validation of select miRNAs by qRT-PCR. All sample values are normalized to *Rnu1a1* expression and relative expression in WT mice treated with BLU3797. (**D,E**) qRT-PCR analysis of *Sfrp1* and *Smad1* levels normalized to *Gapdh* and expression in WT mice treated with BLU3797. . (**F**) SFRP1 protein levels from *MTM1*$^{-/y}$ mice muscle treated with and without BLU3797. (**G**) qRT-PCR of *Sfrp1* expression in C2C12 cells WT or deficient for MTM1 with BLU3797 treatment (final 48 hours of 5 day protocol), values normalized to *Gapdh* and WT untreated cells. (**H**) Western blot of SMAD1 and total actin in lysates from the muscle of *MTM1*$^{-/y}$ mice. (**I**) Quantification of SMAD1 levels shown in panel H; values are normalized to Actin and protein levels in WT mice treated with BLU3797. In

box-and-whisker plots, median (line), mean (symbol), 25-75th quartile range (box), and minimum and maximum (whiskers) are shown. *p≤0.05, **p≤0.01, ***p≤0.001. Comparisons of select miRNAs across BLU3797 dosing regiments were done by unpaired T-test. Comparisons of SFRP1 protein levels were done using Dunnett's correction.

GAPDH, glyceraldehyde-3-phosphate dehydrogenase; miRNA, microRNA; MTM, myotubularin; MTM1, myotubularin 1; PIK3C2B, phosphatidylinositol-4-phosphate 3-kinase catalytic subunit type 2 beta; Q36h, every 36 hours; qRT-PCR, quantitative real-time polymerase chain reaction; SEM, standard error of the mean; SFRP1, secreted frizzled-related protein 1; SMAD1, suppressor of mothers against decapentaplegic protein 1; WT, wild-type.